

**3 - D Hydrodynamic and
Sediment Transport Modelling
of the
St. Clair River near Sarnia**

Jian Ye
University of Windsor

J.A. McCorquodale
University of New Orleans

1997

3-D HYDRODYNAMIC AND SEDIMENT TRANSPORT MODELLING OF ST. CLAIR RIVER NEAR SARNIA

By Jian Ye and J.A. McCorquodale

UNIVERSITY OF WINDSOR

I. INTRODUCTION

The St. Clair River RAP has identified an Area of Concern in the upper St. Clair River between Sarnia Bay and Stag Island. Sediment cores show a narrow strip of contaminated sediments along the Canadian side of the River. The major contaminants include: HCB, HCBP, OCS, organic solvents and Hg. These are practically the result of the past discharges from the Sarnia Chemical Industries. The sediments are a mixture of gravel, sand, silt and clay particles. Most of the central portion of the channel is highly consolidated glacial till which is not contaminated and is highly resistant to erosion.

The flow and stage of the River are subject to long-term and seasonal variations as well as upsets due to storm surges on Lake Huron. A major transient effect on currents is due to the passage of large ships. Approximately 8000 passages occur per year with nearly 15% of these being 1000ft freighters.

A 3D model was developed to simulate the St. Clair River near Sarnia. The purpose of this model was to estimate the bed shear stresses in the areas of the contaminated sediments for a range

of hydraulic and shipping conditions. The purpose of this information was to improve the predictive capability of the IPX model that SUNY (State University of New York at Buffalo) is applying to this AOC.

The 3D hydrodynamic model has been calibrated using the ADCP data collected by Mr. Peter Nettleton of the MOEE. The sediment transport (resuspension and deposition) was verified using the MOEE sediment trap and sediment rod data. The fine sediment deposition, and resuspension functions were developed by Haralampides et al. (1997) using the circular flume facility at Canada Centre for Inland Waters.

II: MODELS DESCRIPTION

(1) Hydrodynamic Model

By using the hydrostatic pressure distribution assumption, the quasi-3D equations derived from the Navier-Stokes equations are written for the multilayered model as follows:

Continuity equation:

$$\frac{\partial u}{\partial x} + \frac{\partial v}{\partial y} + \frac{\partial w}{\partial z} = 0 \quad (1)$$

Momentum equations:

$$\frac{\partial u}{\partial t} + \frac{\partial uu}{\partial x} + \frac{\partial uv}{\partial y} + \frac{\partial uw}{\partial z} = -\frac{1}{\rho_r} \frac{\partial p}{\partial x} + \frac{\partial}{\partial x} (v_h \frac{\partial u}{\partial x}) + \frac{\partial}{\partial y} (v_h \frac{\partial u}{\partial y}) + \frac{\partial}{\partial z} (v_v \frac{\partial u}{\partial z}) + fv \quad (2)$$

$$\frac{\partial v}{\partial t} + \frac{\partial uv}{\partial x} + \frac{\partial vv}{\partial y} + \frac{\partial vw}{\partial z} = \frac{1}{\rho_r} \frac{\partial p}{\partial y} + \frac{\partial}{\partial x} (v_h \frac{\partial v}{\partial x}) + \frac{\partial}{\partial y} (v_h \frac{\partial v}{\partial y}) + \frac{\partial}{\partial z} (v_v \frac{\partial v}{\partial z}) - fu \quad (3)$$

$$0 = -\rho g - \frac{\partial p}{\partial z} \quad \Rightarrow \quad p = p_0 + \int_{z_b}^{H+z_b} \rho g dz \quad (4)$$

Mass transport equation:

$$\frac{\partial C}{\partial t} + \frac{\partial uC}{\partial x} + \frac{\partial vC}{\partial y} + \frac{\partial wC}{\partial z} = \frac{\partial}{\partial x} (A_h \frac{\partial u}{\partial x}) + \frac{\partial}{\partial y} (A_h \frac{\partial u}{\partial y}) + \frac{\partial}{\partial z} (A_v \frac{\partial u}{\partial z}) + S_c \quad (5)$$

where u, v, w = the velocity components in the x, y, z directions in the Cartesian coordinates respectively; p = the water pressure; f = the Coriolis parameter as $2\omega \sin\phi$ where ϕ = the latitude and ω = the angular speed of earth rotation ($f = 0.0001$ rad/s in this study); v_h, v_v = the eddy viscosity coefficients in the horizontal and vertical directions respectively. C = the concentration; S_c = the source term for concentration; A_h, A_v = the eddy viscosity coefficients for C ; $\rho(x, y, z)$ = fluid density; ρ_r = reference fluid density.

In the multilayer model, the governing equations are integrated over each sublayer h_m ($m=1, M$) from z_m to z_{m+1} . Then the sublayer-averaged equations are as follows:

Continuity equation:

$$\frac{\partial}{\partial x} (h\bar{u})_m + \frac{\partial}{\partial y} (h\bar{v})_m + \frac{\partial H}{\partial t} - w_b = 0 \quad (m=M) \quad (6)$$

$$\frac{\partial}{\partial x} (h\bar{u})_m + \frac{\partial}{\partial y} (h\bar{v})_m + w_t - w_b = 0 \quad (m < M) \quad (7)$$

Momentum equations can be written in the following general form:

$$\frac{\partial}{\partial t} (h\phi)_m + \frac{\partial}{\partial x} (h\bar{u}\phi)_m + \frac{\partial}{\partial y} (h\bar{v}\phi)_m = \frac{\partial}{\partial x} (h\Gamma_h \frac{\partial \phi}{\partial x})_m + \frac{\partial}{\partial y} (h\Gamma_h \frac{\partial \phi}{\partial y})_m + S_{\phi m} \quad (8)$$

$$\phi = \bar{u}, \quad \Gamma_h = \nu_h$$

$$S_{\bar{u}m} = (wu)_b - (wu)_t + \tau_{tx} - \tau_{bx} + fvh_m - \frac{\rho_o}{\rho_r} gh_m \frac{\partial H + Z_b}{\partial x} - \int_{z_{m+1/2}}^{H+Z_b} \frac{g\partial\rho}{\rho_r \partial x} h_m dz$$

$$\phi = \bar{v}, \quad \Gamma_h = \nu_h$$

$$S_{\bar{v}m} = (wv)_b - (wv)_t + \tau_{ty} - \tau_{by} - fuh_m - \frac{\rho_o}{\rho_r} gh_m \frac{\partial H + Z_b}{\partial y} - \int_{z_{m+1/2}}^{H+Z_b} \frac{g\partial\rho}{\rho_r \partial y} h_m dz$$

where ρ_o = the surface fluid density. At the free surface,

$$w|_{H+Z_b} = \frac{\partial H + Z_b}{\partial t} + u|_{H+Z_b} \frac{\partial H + Z_b}{\partial x} + v|_{H+Z_b} \frac{\partial H + Z_b}{\partial y} \quad (9)$$

In the present free surface water model, a curvilinear coordinate system (ξ, η) is introduced in the x, y plane to capture the natural irregular geometry of rivers and lakes, i.e.:

$$x(\xi, \eta), \quad y = y(\xi, \eta) \quad (10)$$

the water surface ($z = H + Z_b$), the bottom ($z = Z_b$); H is water depth, Z_b is bed elevation.

By the chain rule, transformation from the Cartesian coordinates (x, y, z, t) to the non-orthogonal curvilinear coordinates (ξ, η, z, t) has the following relations:

$$\xi_x = y_\eta / J, \quad \eta_x = -y_\xi / J, \quad \xi_y = -x_\eta / J, \quad \eta_y = x_\xi / J, \quad J = x_\xi y_\eta - x_\eta y_\xi \quad (11)$$

In the new coordinate system, the velocities are defined as:

$$U = uy_{\eta} - vx_{\eta} \quad , \quad V = vx_{\xi} - uy_{\xi} \quad (12)$$

U, V are called the contravariant velocities which are perpendicular to the η, ξ curvilinear coordinates respectively.

The final governing equations for multilayer model of 3D free surface flows in non-orthogonal curvilinear coordinates using Cartesian velocities as dependent variables can be stated as:

Continuity equation:

$$\frac{1}{J} \left[\frac{\partial}{\partial \xi} (h\bar{U})_m + \frac{\partial}{\partial \eta} (h\bar{V})_m \right] + \frac{\partial H}{\partial t} - w_b = 0 \quad (m=M) \quad (13)$$

$$\frac{1}{J} \left[\frac{\partial}{\partial \xi} (h\bar{U})_m + \frac{\partial}{\partial \eta} (h\bar{V})_m \right] + w_t - w_b = 0 \quad (m < M) \quad (14)$$

Momentum equations:

$$\begin{aligned} \frac{\partial}{\partial t} (h\phi)_m + \frac{1}{J} \left[\frac{\partial}{\partial \xi} (h\bar{U}\phi)_m + \frac{\partial}{\partial \eta} (h\bar{V}\phi)_m \right] - \frac{1}{J} \left(\frac{\partial}{\partial \xi} \left[\frac{h\Gamma_h}{J} \left(\alpha \frac{\partial \phi}{\partial \xi} - \beta \frac{\partial \phi}{\partial \eta} \right) \right]_m + \right. \\ \left. \frac{\partial}{\partial \eta} \left[\frac{h\Gamma_h}{J} \left(\gamma \frac{\partial \phi}{\partial \eta} - \beta \frac{\partial \phi}{\partial \xi} \right) \right]_m \right) + S_{\phi m} \end{aligned} \quad (15)$$

where

$$\alpha = x_{\eta}^2 + y_{\eta}^2 \quad , \quad \beta = x_{\xi}x_{\eta} + y_{\xi}y_{\eta} \quad , \quad \gamma = x_{\xi}^2 + y_{\xi}^2$$

and

Integrating the continuity equation (11) over the depth leads the total depth-averaged equation that can be used to determine the location of free surface :

$$\frac{\partial H}{\partial t} + \frac{1}{J} \left(\frac{\partial H\bar{U}}{\partial \xi} + \frac{\partial H\bar{V}}{\partial \eta} \right) = 0 \quad (16)$$

where the overbars of u, v denotes the sublayer-averaged values of velocities; the double overbars on U, V indicate the total depth-averaged values of U, V .

Subtracting Eq. (16) from Eq. (13) gives the solution of w_b at layer M :

$$w_b = \frac{1}{J} \left\{ \frac{\partial}{\partial \xi} [(h\bar{U})_m - H\bar{U}] + \frac{\partial}{\partial \eta} [(h\bar{V})_m - H\bar{V}] \right\} \quad (m=M) \quad (17)$$

$$w_b = w_t + \frac{1}{J} \left[\frac{\partial}{\partial \xi} (h\bar{U})_m + \frac{\partial}{\partial \eta} (h\bar{V})_m \right] \quad (m < M) \quad (18)$$

(2) Sediment Transport Model

Considering the interaction between the sand bed and water column (Fig. 1), the sediment transport equation can be expressed as:

$$\text{UNSTEADY} + \text{CONV.} = \text{DIFF.} + \text{SOURCE} + E \uparrow + D \downarrow$$

$$\begin{aligned} \frac{\partial (h\bar{C})_m}{\partial t} + \frac{1}{J} \left[\frac{\partial}{\partial \xi} (h\bar{UC})_m + \frac{\partial}{\partial \eta} (h\bar{VC})_m \right] = \frac{1}{J} \left\{ \frac{\partial}{\partial \xi} \left[\frac{h\Gamma_h}{J} \left(\alpha \frac{\partial \bar{C}}{\partial \xi} - \beta \frac{\partial \bar{C}}{\partial \eta} \right) \right]_m + \right. \\ \left. \frac{\partial}{\partial \eta} \left[\frac{h\Gamma_h}{J} \left(\gamma \frac{\partial \bar{C}}{\partial \eta} - \beta \frac{\partial \bar{C}}{\partial \xi} \right) \right]_m \right\} + S_{cm} + E_m \uparrow - D_m \downarrow \quad (19) \end{aligned}$$

where $D\downarrow$ =settling and deposition term; $E\uparrow$ = resuspension and erosion term.

$$E_m\uparrow = \frac{\partial}{\partial z} (A_v \frac{\partial C}{\partial z} - wC) \quad ; \quad D_m\downarrow = -(W_s C) \quad (20)$$

Sediment characterization:

(A) Settling and Deposition ($D\downarrow$)

$$D\downarrow = P W_s C \quad (21)$$

$$\tau > \tau_d \quad P = 0$$

$$\tau \leq \tau_d \quad P = 1 - \tau/\tau_d$$

W_s =settling velocity (8.5×10^{-5} m/s); τ_d = critical shear stress for deposition; P = probability of deposition by considering the fact that if shear stress is greater than τ_d , there will be no deposition (Lick et al., 1994).

(B) Resuspension and Erosion ($E\uparrow$) (see Report by Haralampides et al. (1997) on Sediment transport)

$$(\tau - \tau_c) \leq 0 \quad E\uparrow = 0 \quad (22)$$

$$0 < (\tau - \tau_c) \leq 1.4 \quad E\uparrow = 0.18 (\tau - \tau_c)^{4.8}$$

$$(\tau - \tau_c) > 1.4 \quad E\uparrow = 3.753(\tau - \tau_c) - 4.35$$

τ_c = critical shear stress for erosion. Considering the consolidation and armouring effects of sediment, τ_c increases with the sediment thickness. This variation is shown in Fig. 2. A

comparison of Eq.(22) with the data is shown in Fig. 3.
(Haralampides, 1997).

(3) Eddy Viscosity

The horizontal eddy viscosity ν_h is determined by:

$$\nu_h = \lambda U_* H \quad (23)$$

The vertical eddy viscosities can be described by the empirical profiles of the mixing layer theory.

$$\nu_v = \kappa U_* z(1-z/H) \quad (24)$$

In present paper, $\lambda=0.2$, $\kappa=0.4$.

(4) Numerical Scheme

The set of equations is solved by using the efficient two-step implicit fractional method. A non-staggered grid system is used to save the memory and CPU time.

To overcome the deficiency of numerical diffusion associated with the first order upwind schemes, e.g. hybrid and power-law schemes, the second order upwind scheme of Roe (Ye and McCorquodale, 1997b) has been incorporate in the code to discretize the convective terms. Applications show that the accuracy of predictions will be improved by the Roe's scheme when the convective effect plays an important role in the momentum transportation.

III. MODEL CALIBRATION

(1): Hydrodynamic Part

The computational domain of the St. Clair River is between downstream of the Black River to upstream of the Stag Inland, as shown in Fig. 4. Figs. 5, 6 give the grid and modelled bathymetry(NOAA, 1984) of the domain, respectively.

The flow conditions of Sept.7 1994 measured by MOEE were used for the model calibration. The locations of the measured spots and the depth-averaged velocities are shown in Figs. 7, 8, respectively. Manning's Roughness (0.022-0.03) is based on Water Surface Profile by Great Lakes Hydraulics and Hydrology Branch, U.S. Army Corps. of Engineer, Detroit District.

Simulations of the depth-averaged and surface velocity distributions are given in Figs. 9 and 10, respectively. Figure 11 presents the zoom view of the surface vector field near the interested area.

Some typical vertical distributions of velocity are given in Fig. 12, which show a reasonably good agreement with the data of P. Nettleton.

(2): Mass Transport

Based on the MOEE MISA study published in 1987, the 1986 loadings of HCB are given in Table 1 for the outfalls shown in Fig. 13. The results of two schemes (Power-law and Roe's scheme) are presented for comparison with the measurements in Table 2 and Fig. 14. It is apparent that the Roe's scheme presents a better agreement due to its higher accuracy. Figures 15, 16 show the

concentration pattern of HCB for the 1986 loading.

(3) : Sedimentation

(A) Pure deposition

[Data: MOEE sediment trap measured in 95/07/25, after 49 days;

data source: MOEE]

By only taking account of the deposition part of Eq.(19), the distribution of pure deposition is shown in Fig. 17. Sediment traps were placed along Canadian side, as indicated in Fig. 17. There were two to three traps placed at each spot. Basically, various sizes of sediment could deposit in a trap, but the model developed in the study only predicted the fine sediment transport. A comparison of the measured fine sediment and the modelled fine sediment deposition is given in Table 3 and Fig. 18. The simulations represent reasonably accurate results. A notable difference can be observed at Station 96 (the last station), where a significant increment in the amount of sediment was detected in the field while the model gave consistent results with the sediment in three upstream stations. One possible reason is because of the ship docking effects (there is a dock for relatively small ships between Station 74 and 96). The ship propeller turbulence would cause significant shear stress in the near shore region, which may have contributed a large amount of sediment being resuspended, some of which would have deposited in the downstream trap (Station 96). Also, the effect of induced currents due to the passage of large ships may have been more important at this station.

(B) Net erosion

[Data: MOEE rod data measured between 94/06/24 and 94/07/19, 26

days; data source: MOEE]

Rods were placed in the channel bed along the Canadian side extending into the St. Clair River from 30 to 65 m. Simulations of net erosion was performed for the conditions that existed during the field sampling. Distributions of net erosion and net deposition areas are given in Figs. 19 and 20, respectively. During that period, the St. Clair River experienced net erosion over most of the area, except for some near shore areas especially in the harbour regions. Figure 21 shows the comparison of the simulation and measurement. The field data give a large range of variation, while the model presents a similar trend to the observations, i.e. having the same sign(positive or negative) of net erosion, but smaller magnitudes. Two reasons can explain this phenomenon: first is because the model only takes account of the fine sediment part in comparison with full range of sizes of sediment in movement in the field; second is due to the ship passage and docking effect that would cause significant disturbance of sediment.

(4) Wind Effect

Wind shear stress at the water surface can be determined by(Wu, 1975) :

$$\tau_w = C_w \rho_w W_w^2 \quad (25)$$

where $C_w = (0.75 + 0.067W_w) * 10^{-3}$, W_w = wind speed(m/s), ρ_w = air density.

Applications:

(A) [Data: AES July 25, 1995, 49 days, strongest wind period:
13 h, average speed: $W_w = 32$ km/h, Direction: NORTH]

Figure 22 shows the distribution of increase in the bed shear stress due to this wind speed ($0 \sim 0.048 \text{ N/m}^2$). There is very little impact on shear stress for this wind condition. However, there may be an increase in River Flow due to setup in Lake Huron.

(B) Typical hydraulic flows in the St. Clair River

(I) 10% of Probability of being less than $Q_{10} = 4780$ CMS
(lower decide)

(II) 50% of Probability of being less than $Q_{50} = 5540$ CMS
(median decide)

(III) 90% of Probability of being less than $Q_{90} = 6240$ CMS
(upper decide)

with typical setup due to a wind speed of 20km/h from the NORTH.

Results of the distribution of shear stress are calculated for the potential capability of the resuspension-deposition process. Figures 23 to 25 show the distribution of shear stress under Q_{10} , Q_{50} , Q_{90} , respectively. Without detailed information of the bottom sediment, it is impossible to give an exact amount of resuspension/deposition. However, from Eqs. (22) and (23), it is possible to estimate the range of capacities for resuspension based on the shear stress distribution. The distributions of maximum and minimum resuspension rate for Q_{50} are shown in Figs. 26 and 27 respectively. For the minimum rate it was assumed that τ_c was maximum, and for the maximum rate it was assumed that τ_c was minimum, as shown in Fig. 2. The surface vector field for Q_{50} is presented in Fig. 28.

(C) [Extreme wind 1:100 year return period, Speed 100 km/h,

Direction: NORTH, Lake Huron Setup was assumed to be 0.5 m]. The near surface flow field for Q50 is given in Fig. 29. In comparison with Fig.20, the currents shift significantly to Canadian side in the case of an extreme wind. Figure 30 illustrates the distribution of the increment in the bed shear stress due to the extreme wind, which shows changes in the range of 0- 2.1 N/m².

(5) Shipping effect

While a ship is upbound in the shipping channel, it causes transient increase in the river current and an associated incremental change in the bottom shear stress increment that may affect the sediment transport. The increment in shear stress is estimated by applying the BERNOULLI energy conservation equation for a ship passage in the present study reach, i.e.

$$\delta = y_1 - y_2 = \alpha_2 \frac{(V_b + V_w + \Delta V)^2}{2g} - \alpha_1 \frac{(V_b + V_w)^2}{2g}$$

$$\Delta V = \frac{(V_b + V_w)A_w}{(A_w - A_s - \delta B)} - (V_b + V_w)$$

$$\lambda = \frac{\tau}{\tau_0} = \left(\frac{V_w + \Delta V}{V_w} \right)^2$$

τ_0 = the bottom shear stress without shipping effect; τ = the bottom shear stress with shipping effect;

where V_b = upbound shipping speed; V_w = the current velocity; B = the river width; y_2, y_1 = the water depths with and without shipping, respectively; δ = depth drawdown due to shipping; α_2, α_1 = momentum correction coefficients (approximately equal to 1.0

here). A_w, A_b = the cross section areas of the river and ship, respectively.

Application to the St. Clair River

Conditions

(A) Two typical size of ships are considered in the shipping channel:

S10: BEAM=105 ft; LENGTH=1000ft

S7 : BEAM=70 ft; LENGTH=720ft

Upbound speed $V_b=12\text{mph}=5.3633 \text{ m/s}$, V_w, A_w and B are calculated by the 3D model.

(B) Hydraulic conditions

Typical hydraulic flows in the St. Clair River

(I) Q10=4780 CMS; (II) Q50=5540 CMS; (III) Q90=6240 CMS.

with typical wind speed 20km/h (from NORTH)

(C) Draft of the ships (H_d) at different Q

(I) Q10: $H_d=25 \text{ ft}$; (II) Q50: $H_d=26.5 \text{ ft}$; (III) Q90: $H_d=28 \text{ ft}$

$$A_b = \text{BEAM} \times H_d$$

Results:

Table 4 gives the results of depth change δ and the ratio of shear stresses ($\lambda=\tau/\tau_0$) due to shipping effect. For S10 class, the depth drop is 14-50cm, the ratio of shear stress is 1.95-2.9, depending on the discharges and locations. Similar conclusion can be drawn for S7 class, where the depth drop is 5.5-23.2cm and the ratio of shear stress is 1.5-1.9. So the larger ships could have

a severe severe impact on the resuspension of sediment. The flume studies by Haralampides et al.(1997) showed that the bed resuspension responded very quickly to rapid changes in applied shear; the log time was less than 20 seconds in the laboratory flume.

(5) Advantages of the Present 3D model

The model developed here is quite robust and efficient. The basic information required are:

- (A) Geometric data: the river bathymetry, shoreline, location of discharge or hot spots.
- (B) Hydrodynamic data: flow Discharge Q , water elevation at downstream, wind Speed W_w (available at airport)
- (C) Mass and sediment data: contaminant sources Q_0 , bottom sediment conditions.

REFERENCES

1. Ye, J. and McCorquodale, J.A.(1995), 'Notes on the Hydrodynamic / Water Quality Modelling of Western Lake Erie', Research Report to Great Lakes Institute of Environmental Research, University of Windsor.
2. Ye, J. and McCorquodale, J.A.(1997a), '3D Numerical Modelling of Mass Transport in Curved Channels', in Press, Canadian J. of Civil Engineering, CSCE.
3. Ye, J. and McCorquodale, J.A.(1997b), ' Depth-averaged Hydrodynamic Model in Curvilinear Collocated Grid', J. Hydraulic Engrg., ASCE, 123(5), 380-388

4. Lick, W., Lick, J. and Ziegler, C.K. (1994), 'The resuspension and transport of fine-grained sediment in Lake Erie', J. Great Lakes Res., 20(4), 599-612.
5. Johnson, B.H., et.al (1993), 'Validation of Three-Dimensional Hydrodynamic Model of Chesapeake Bay', J. of Hydr. Engrg., ASCE, 119(1), 2-20.
6. Jin, X and Kranenburg, C (1993), 'Quasi-3D Numerical Modeling of Shallow-water Circulation', J. of Hydr. Engrg., ASCE, 119(4), 458-472.
7. Haralampides K. and McCorquodale, J.A. and Krishnappan, B. (1997), 'Experimental Study of St. Clair River Sediments', Report to MOEE RAP
8. Wu, J. (1975), 'Wind-induced drift currents', J. Fluid Mechanics, V.68, Part1, pp.49-70.

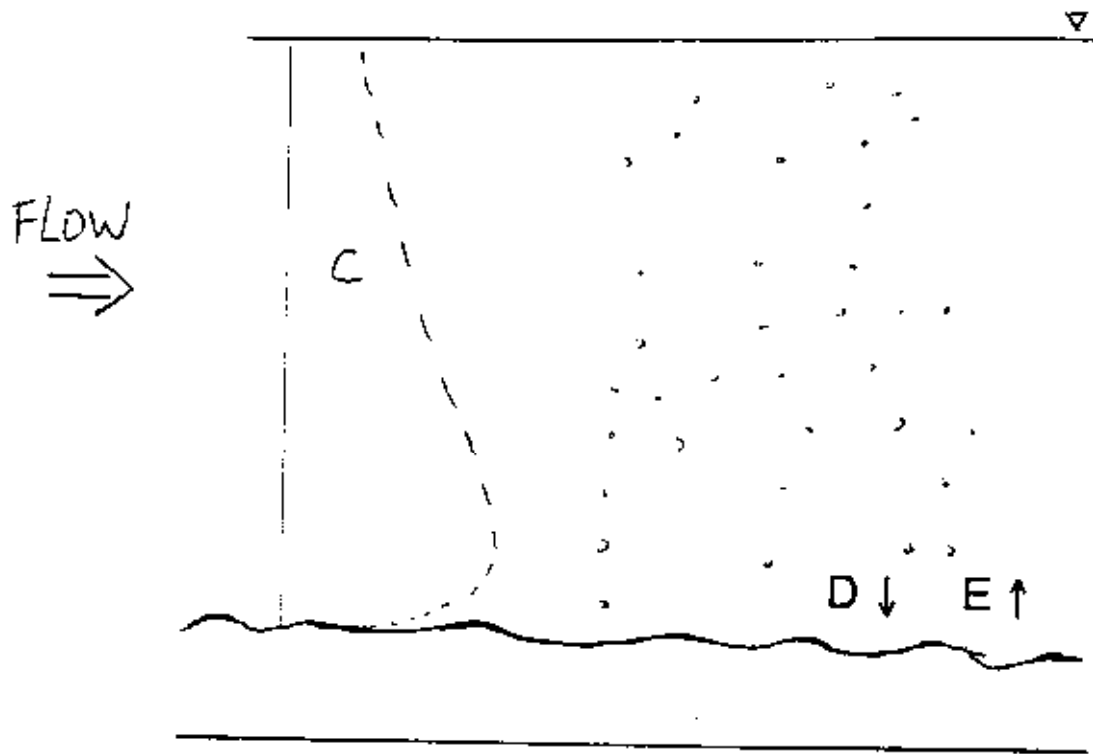


Figure 1 Illustration of deposition and erosion

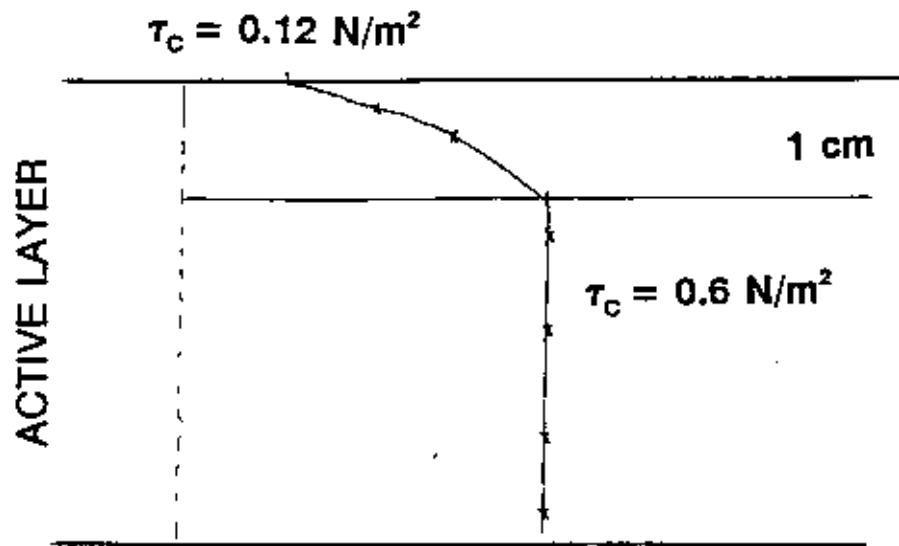
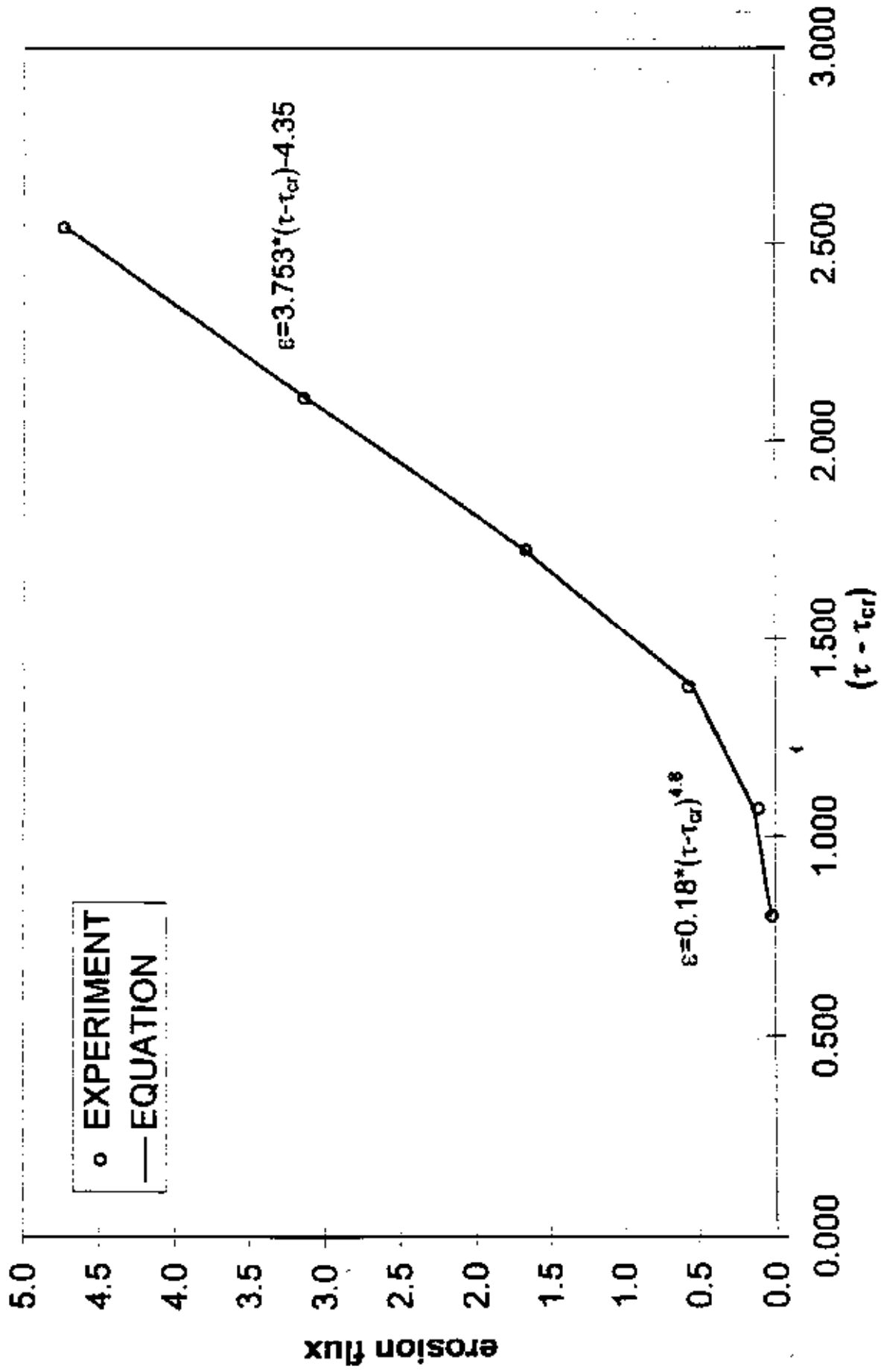


Figure 2 Variation of critical shear stress for erosion

Figure 3 Comparison of erosion flux with data and Eq.(22)



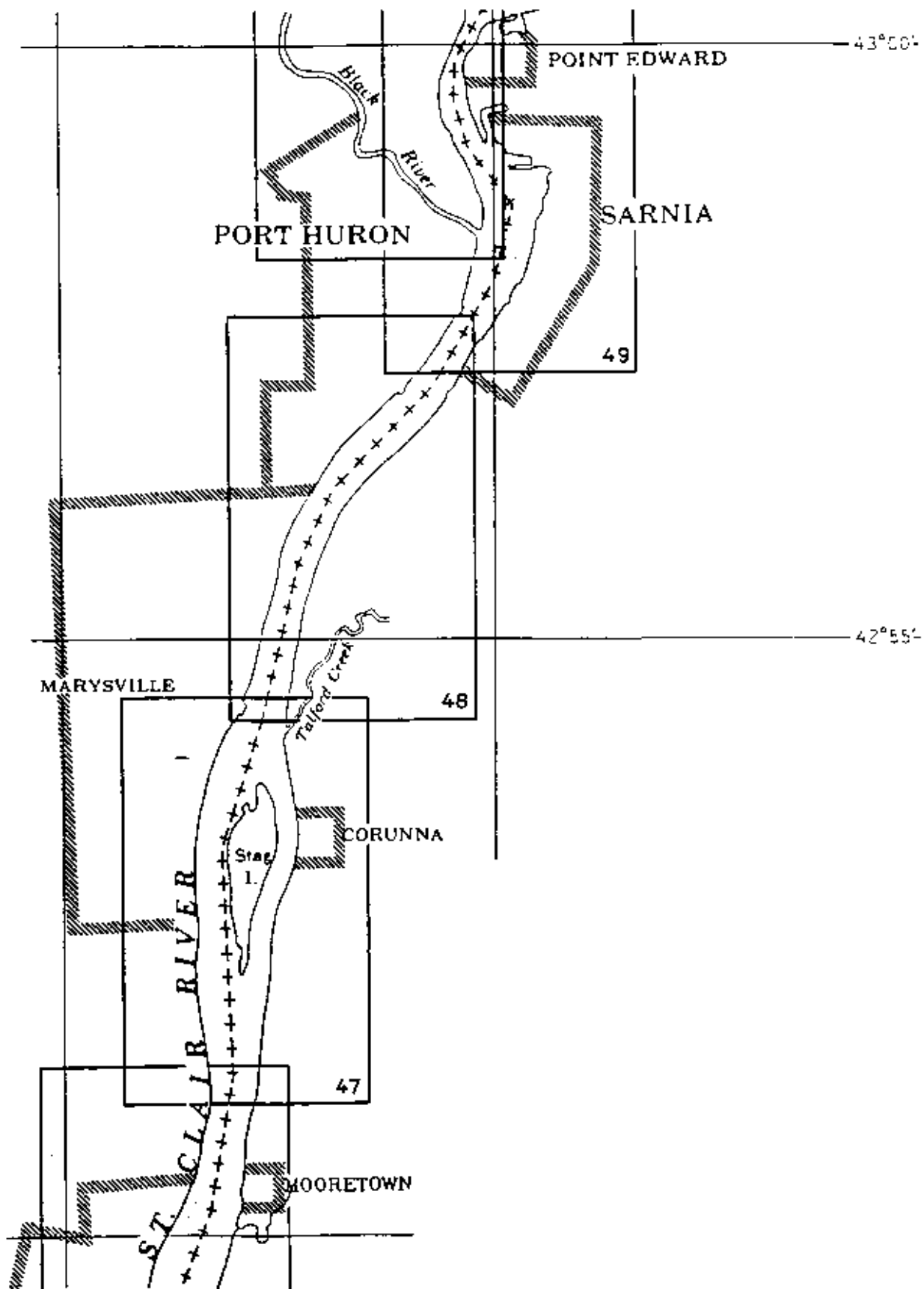


Figure 4 St. Clair River near Sarnia

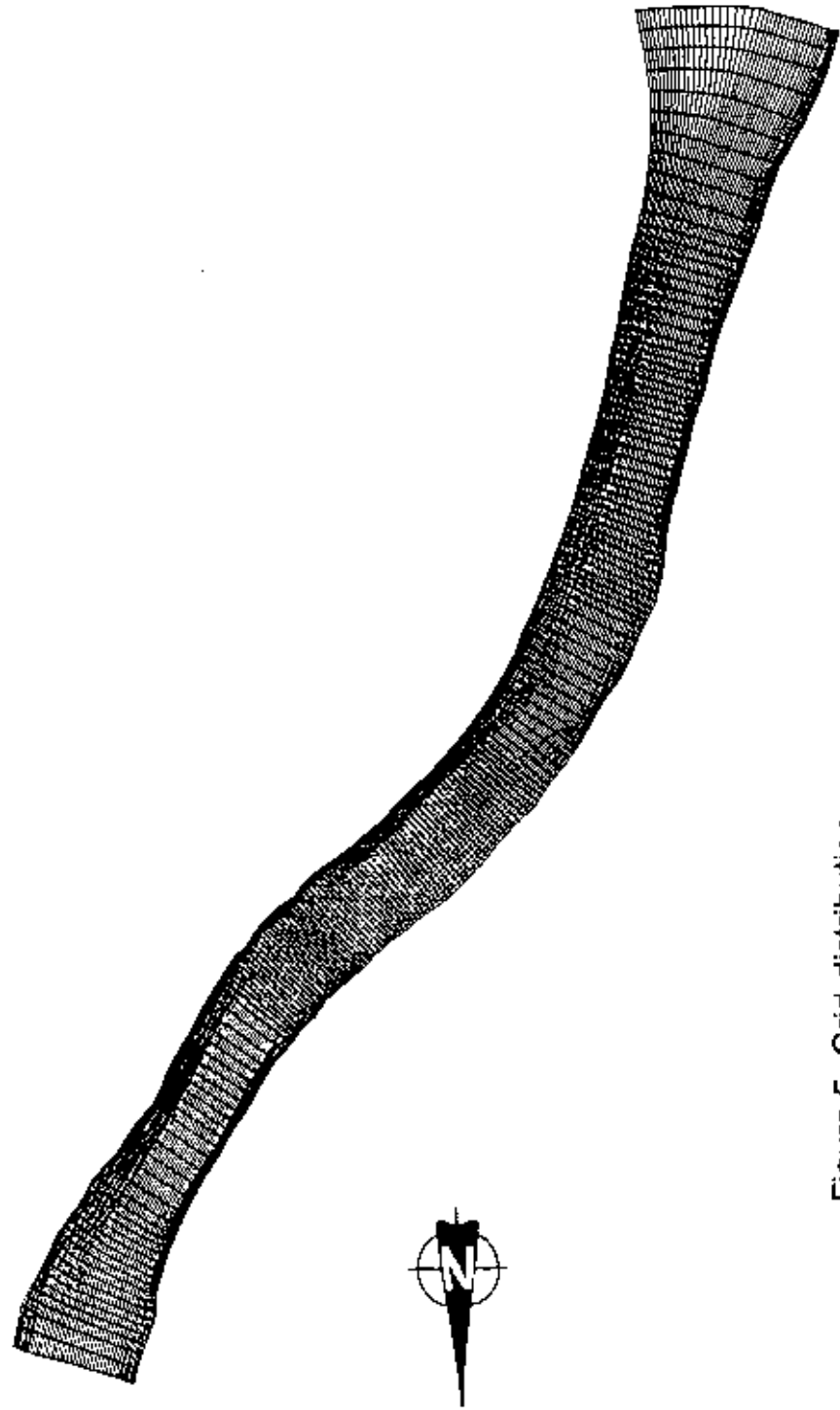


Figure 5 Grid distribution

unit: m

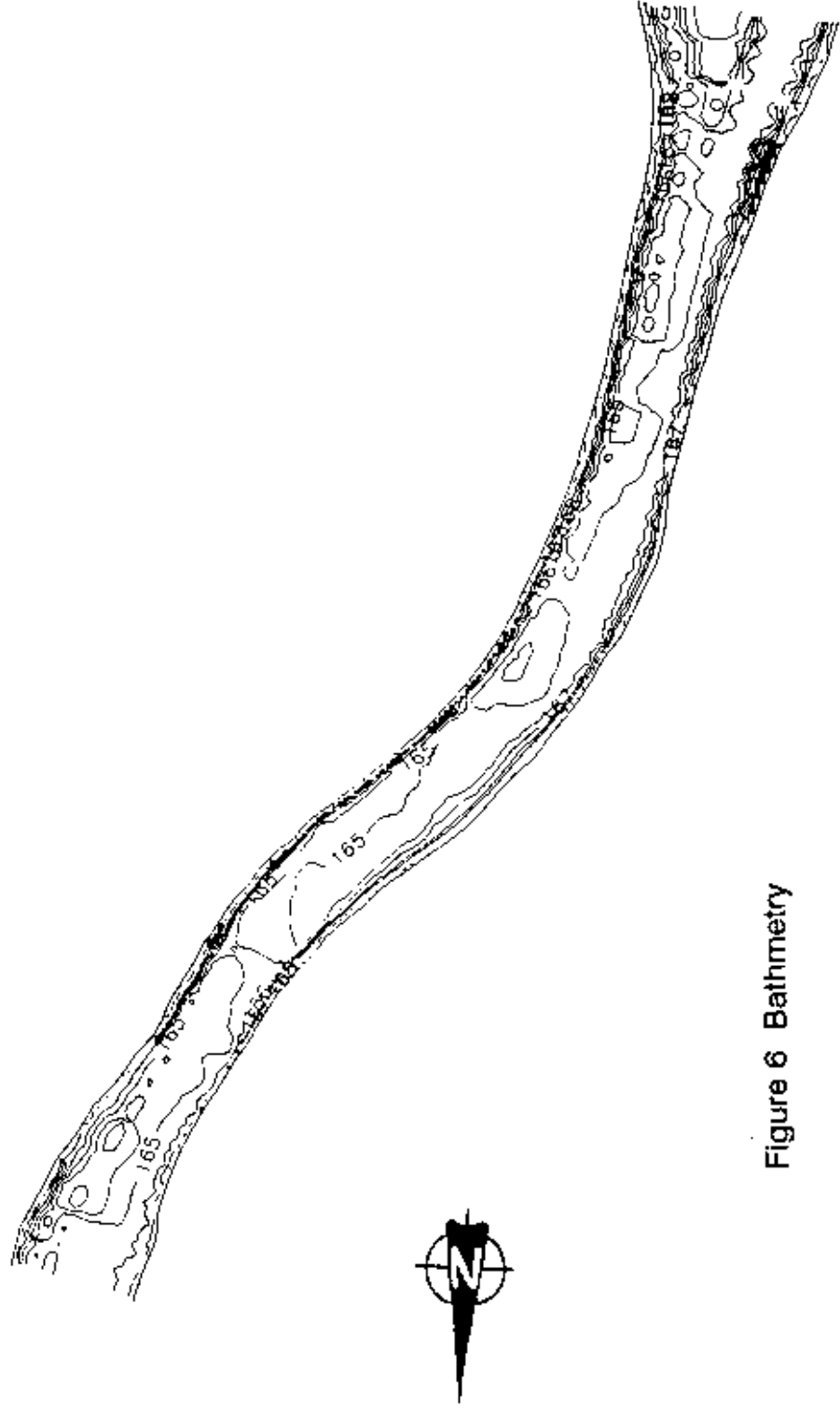


Figure 6 Bathymetry



Figure 7 Location of current measurement

Figure 8 Measured depth-averaged velocity field

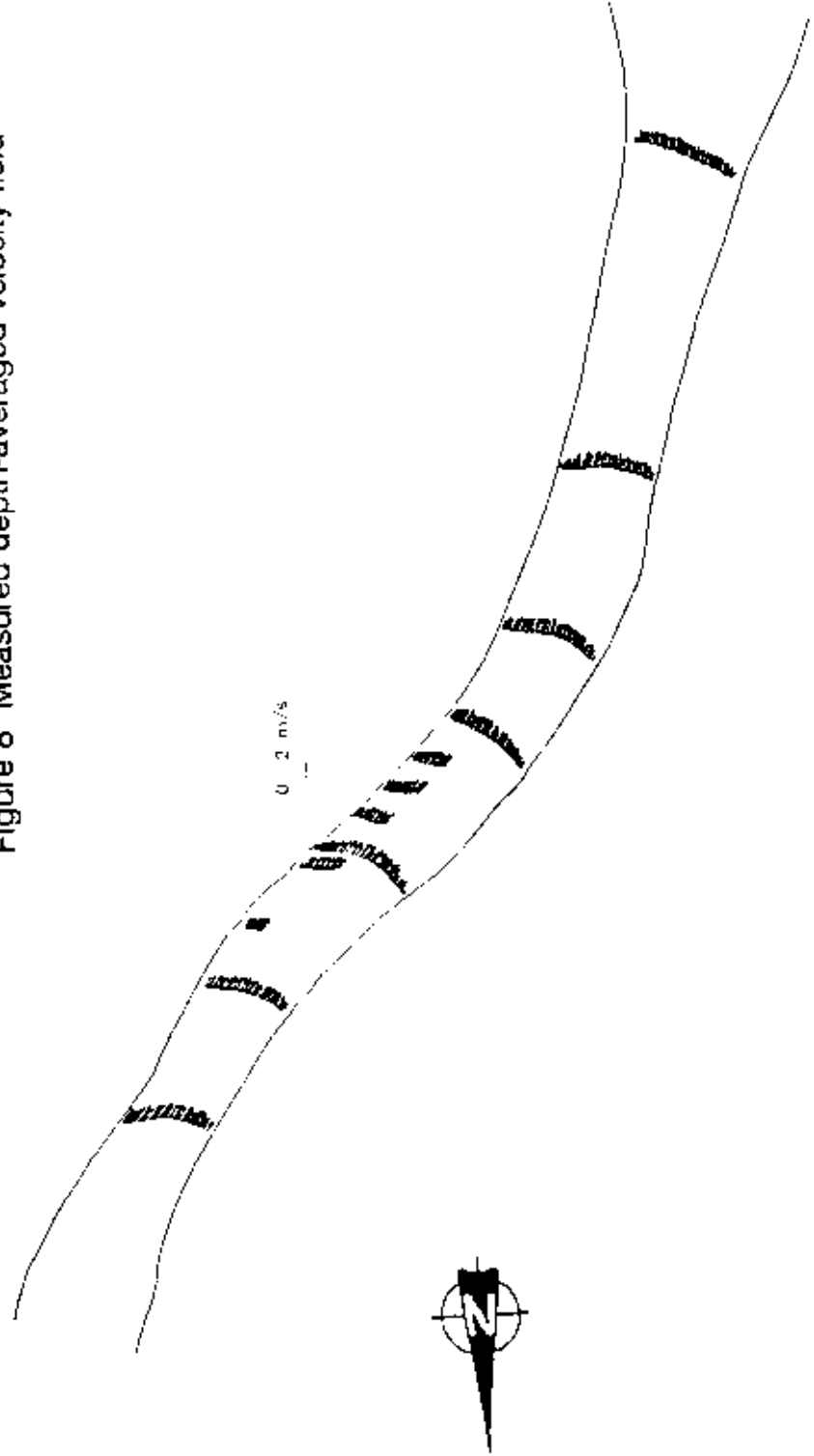


Figure 9 Simulated depth-averaged velocity field

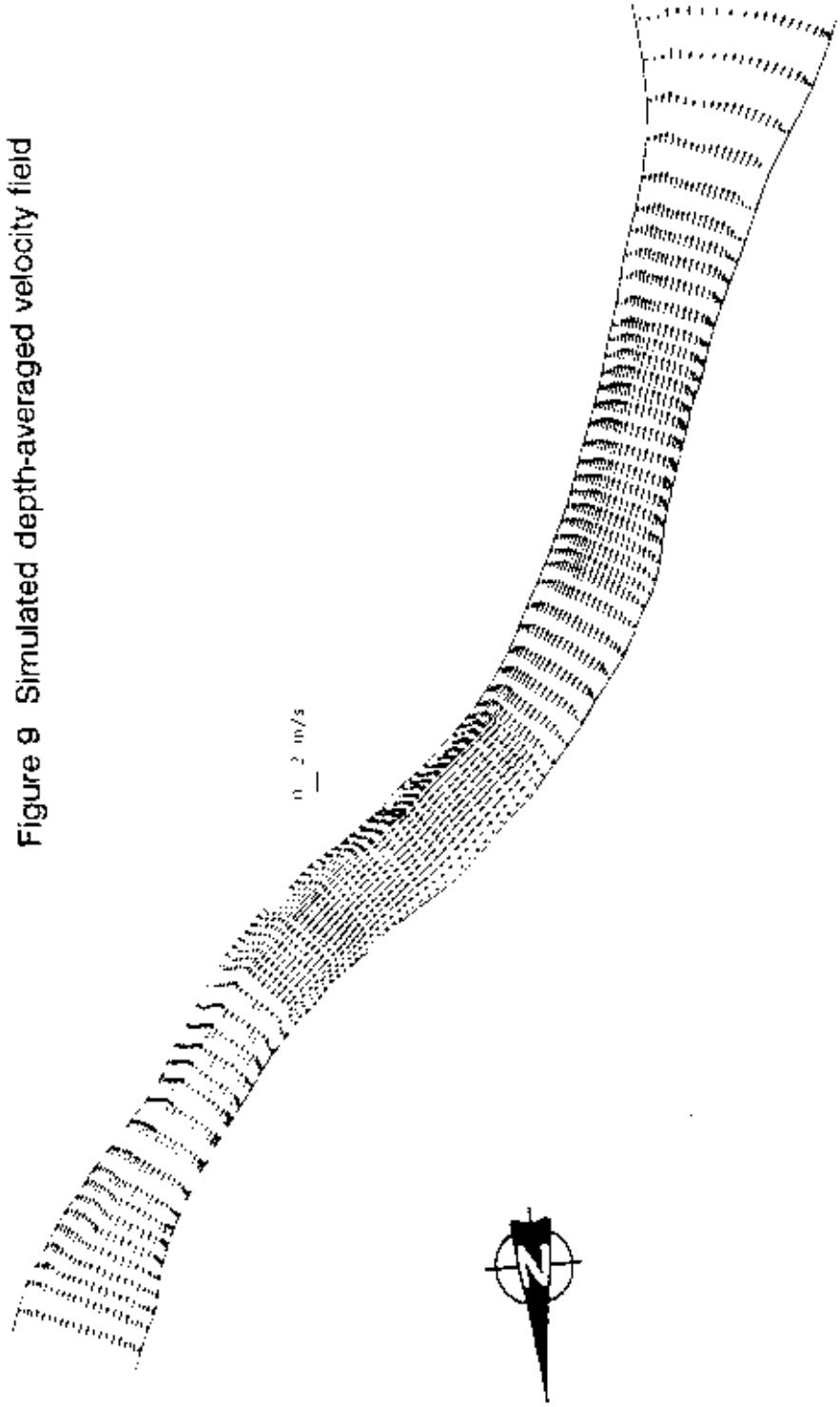


Figure 10 Simulated surface velocity field

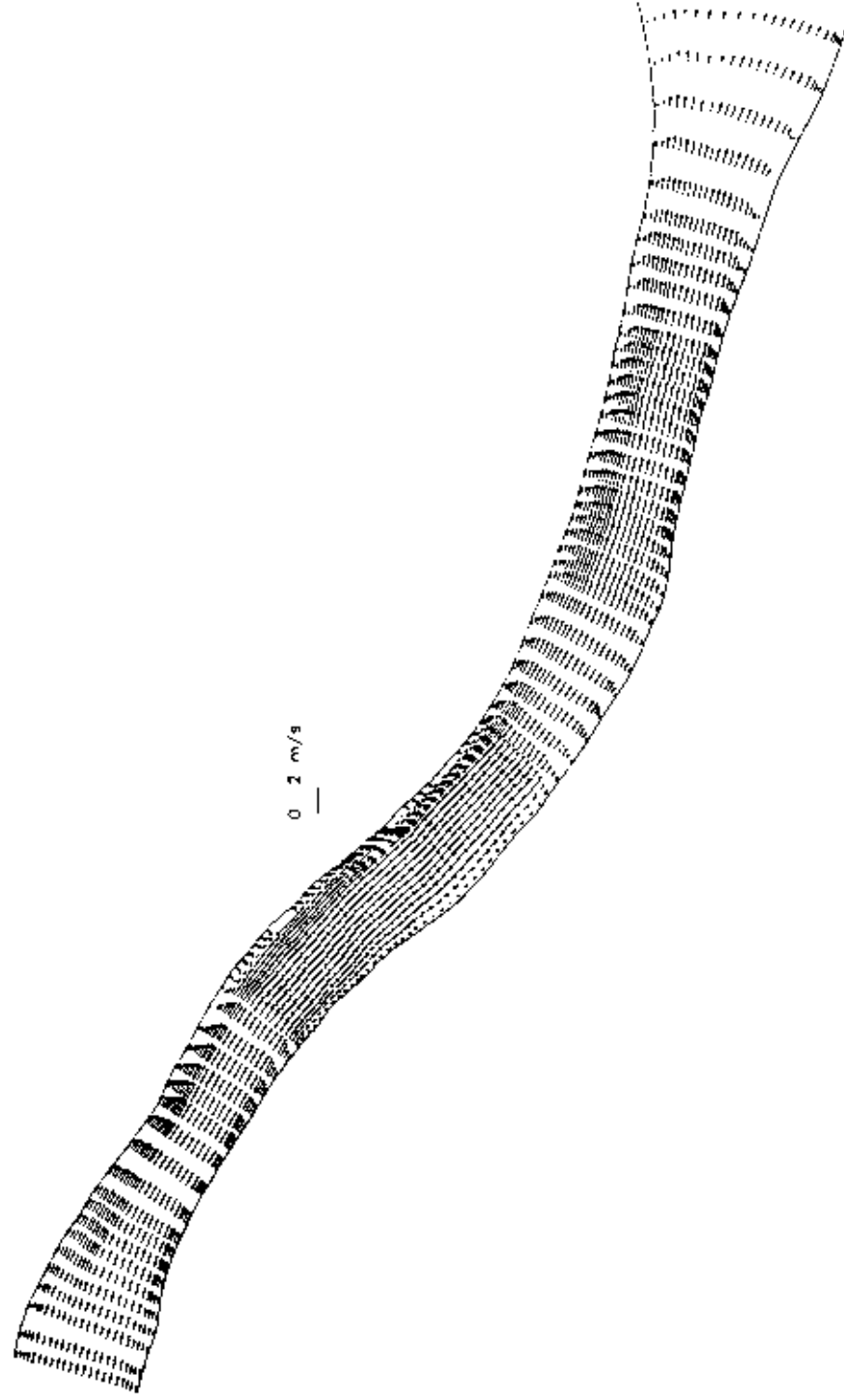


Figure 11 Zoom view of surface velocity field

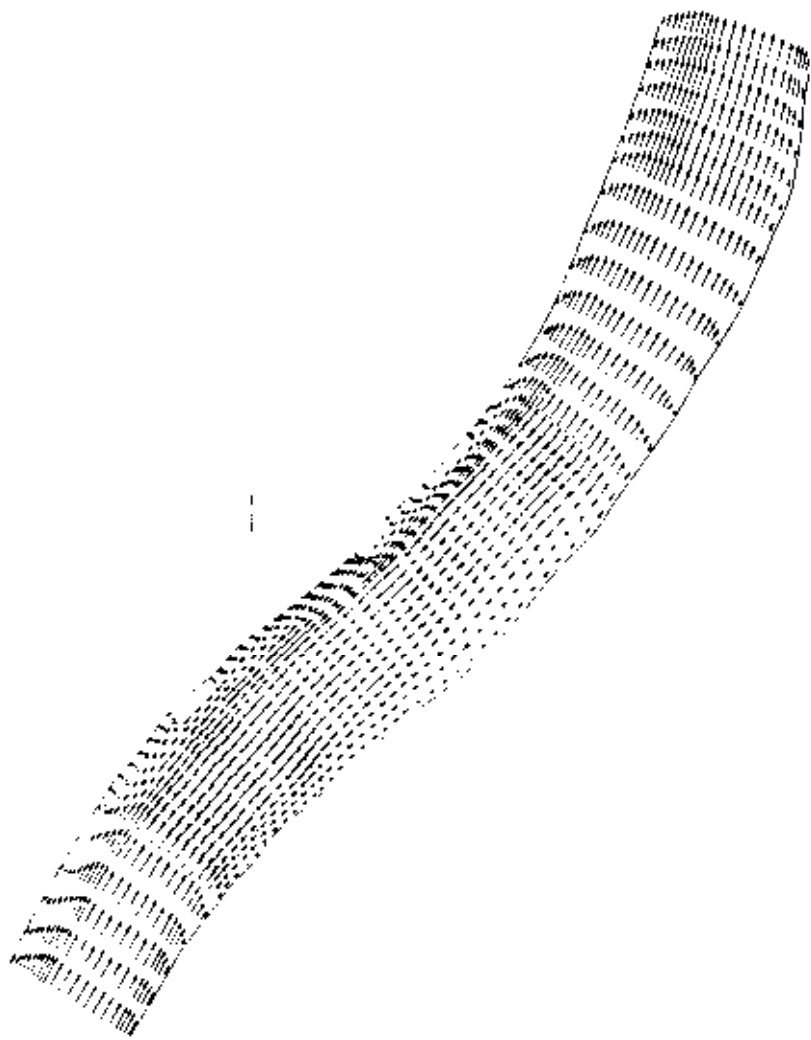


Figure 12 Comparison of vertical distribution of velocity at selected locations

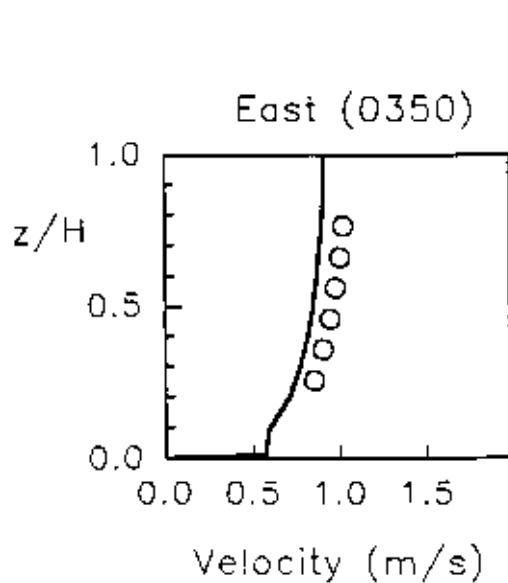
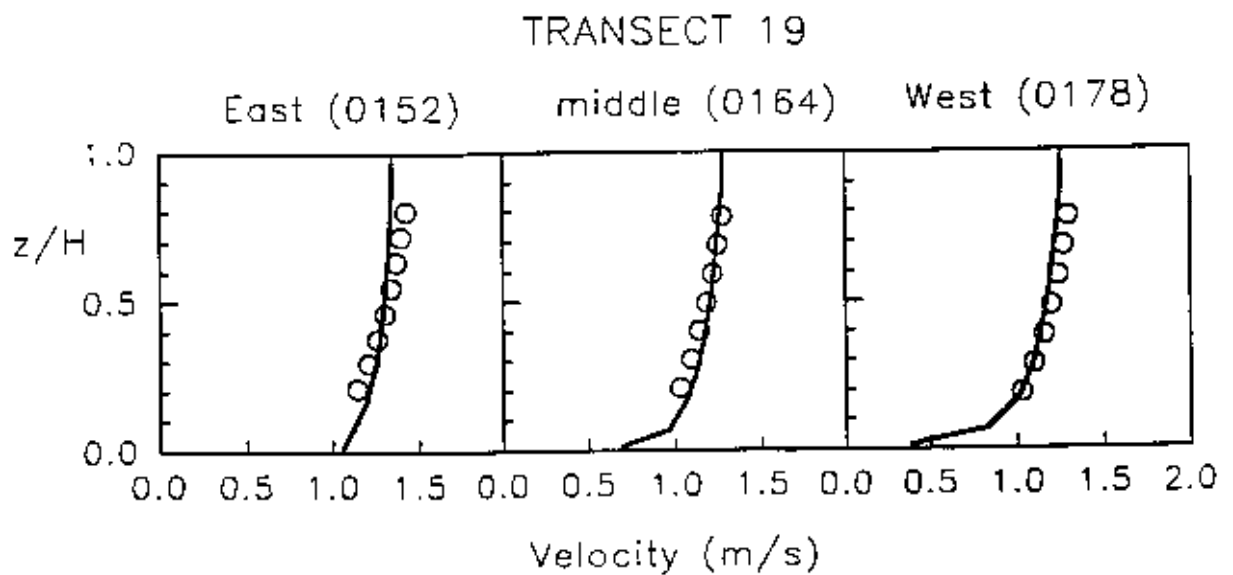
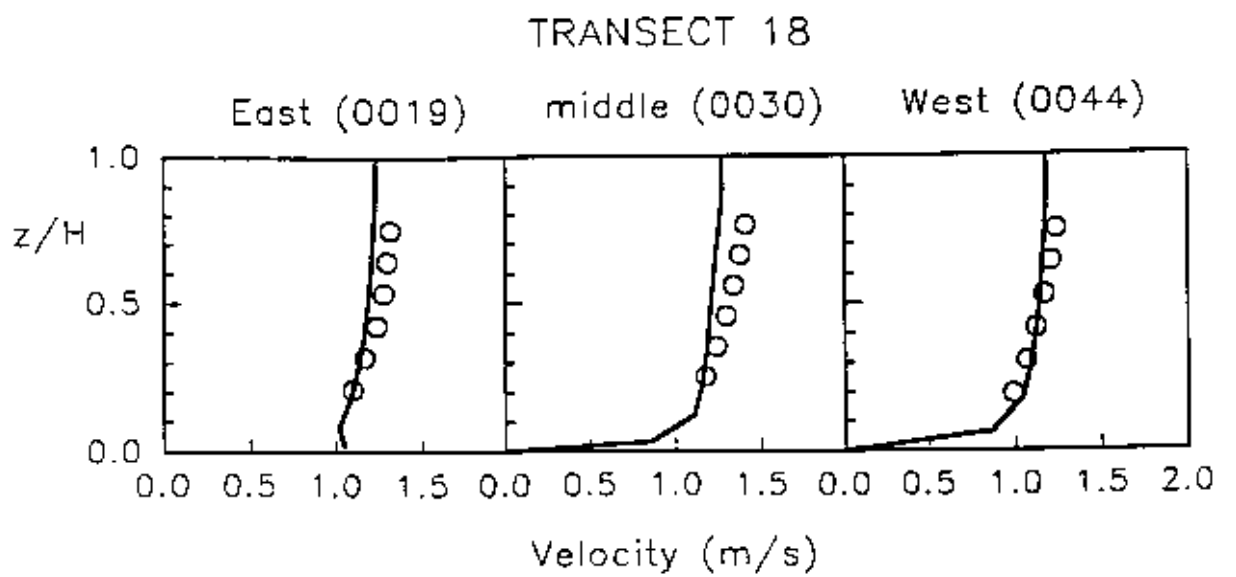
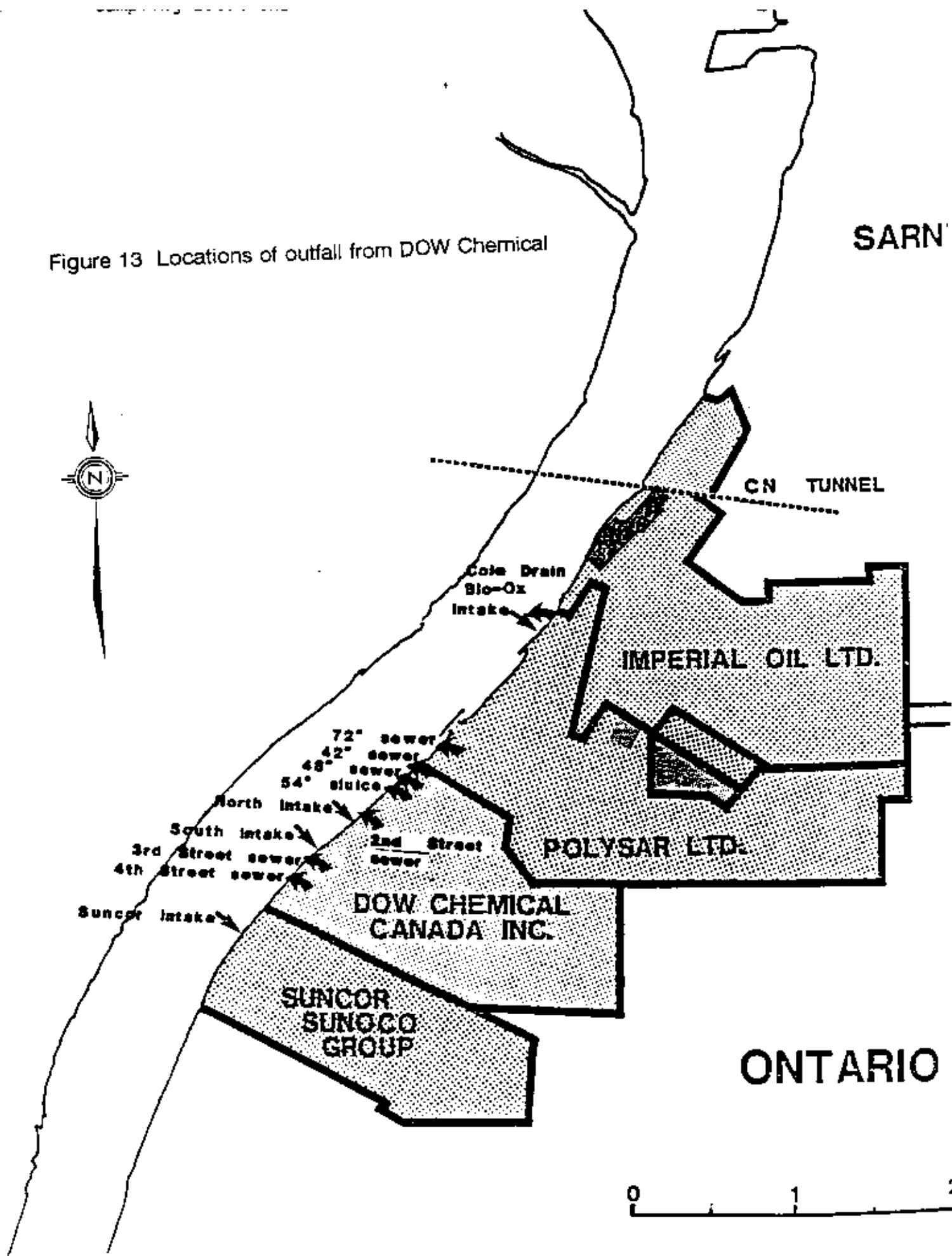


Figure 13 Locations of outfall from DOW Chemical



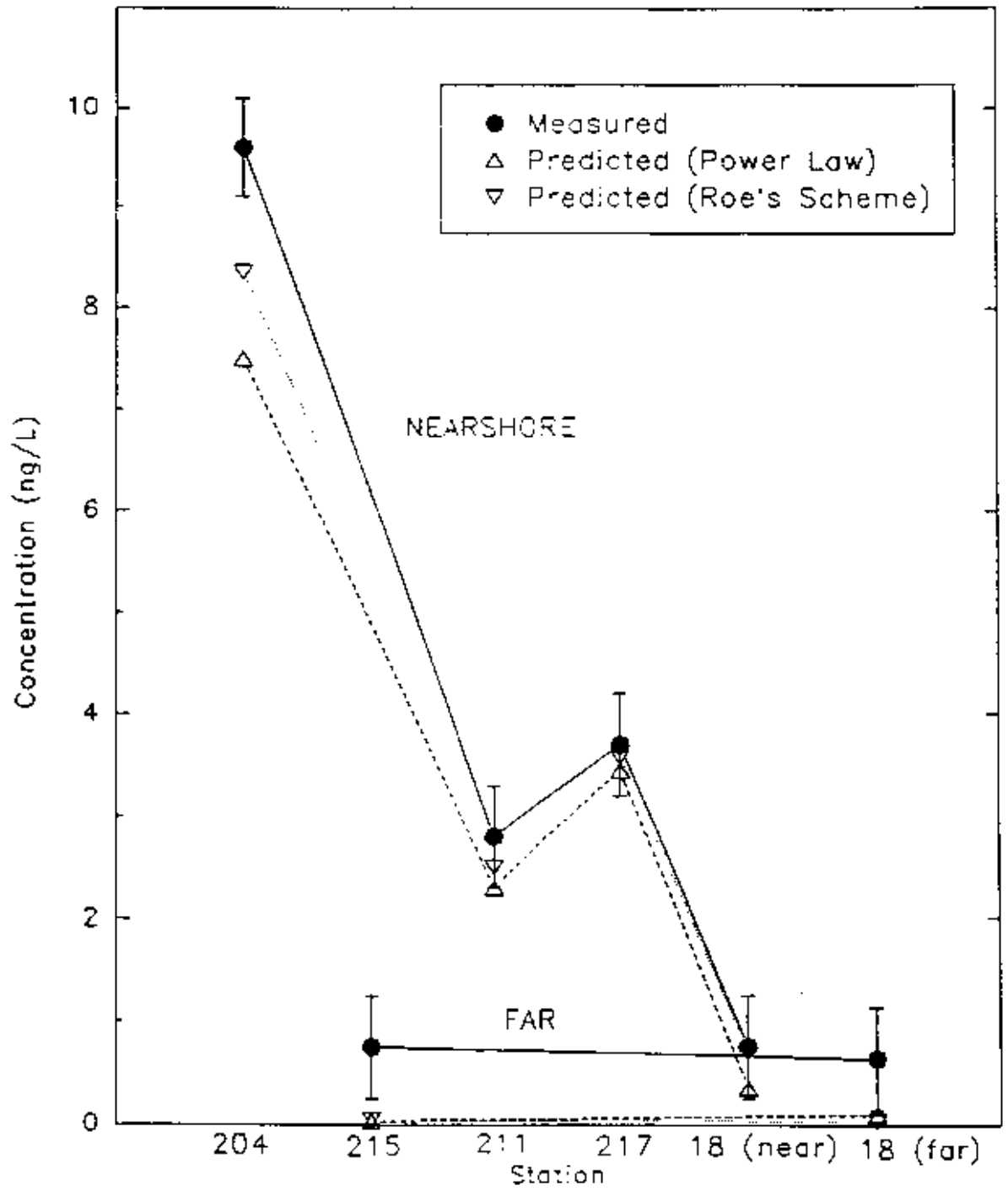


Figure 14 Comparison of simulations and data for mass transport

Figure 15 Simulated surface concentration distribution

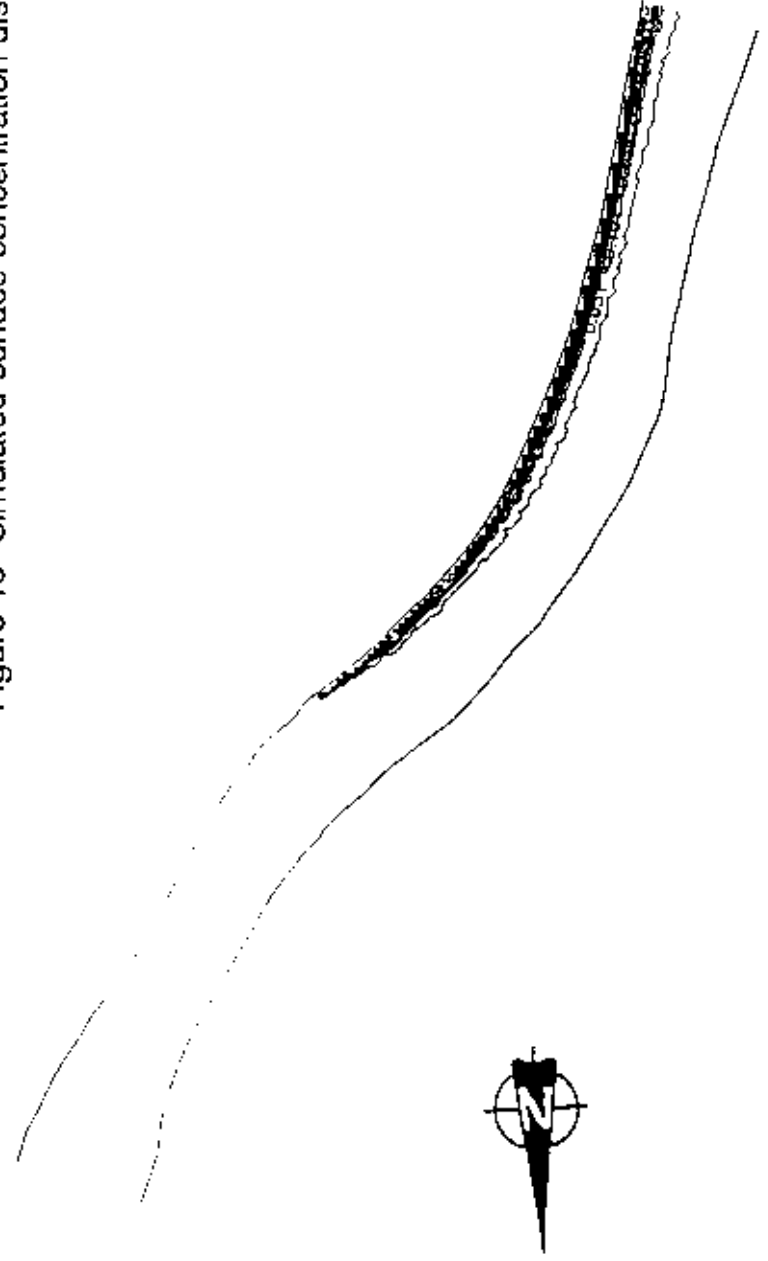


Figure 16 Zoom view of surface concentration distribution

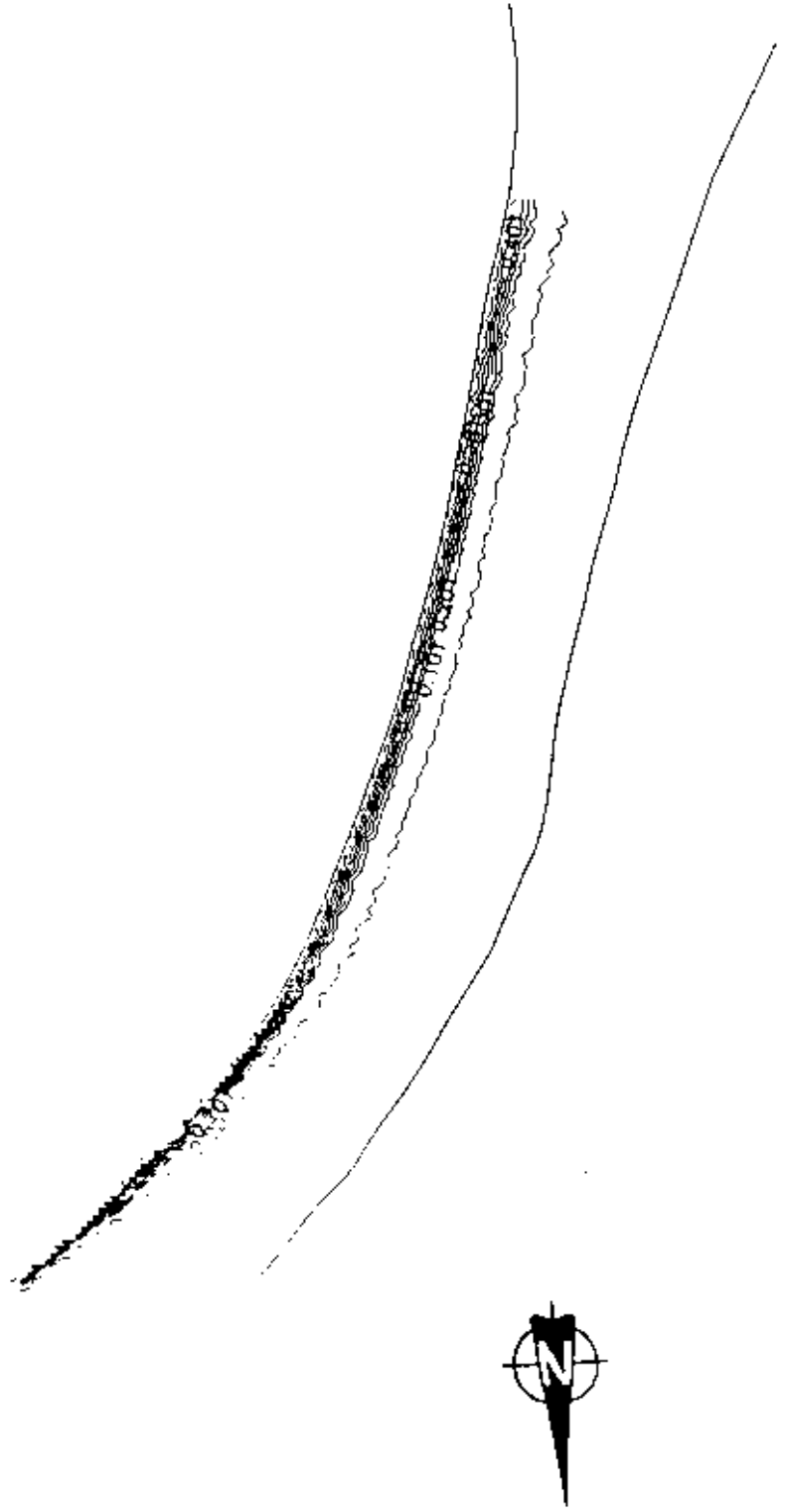


Figure 17 Deposition area after 49 days, measured on 95/07/25

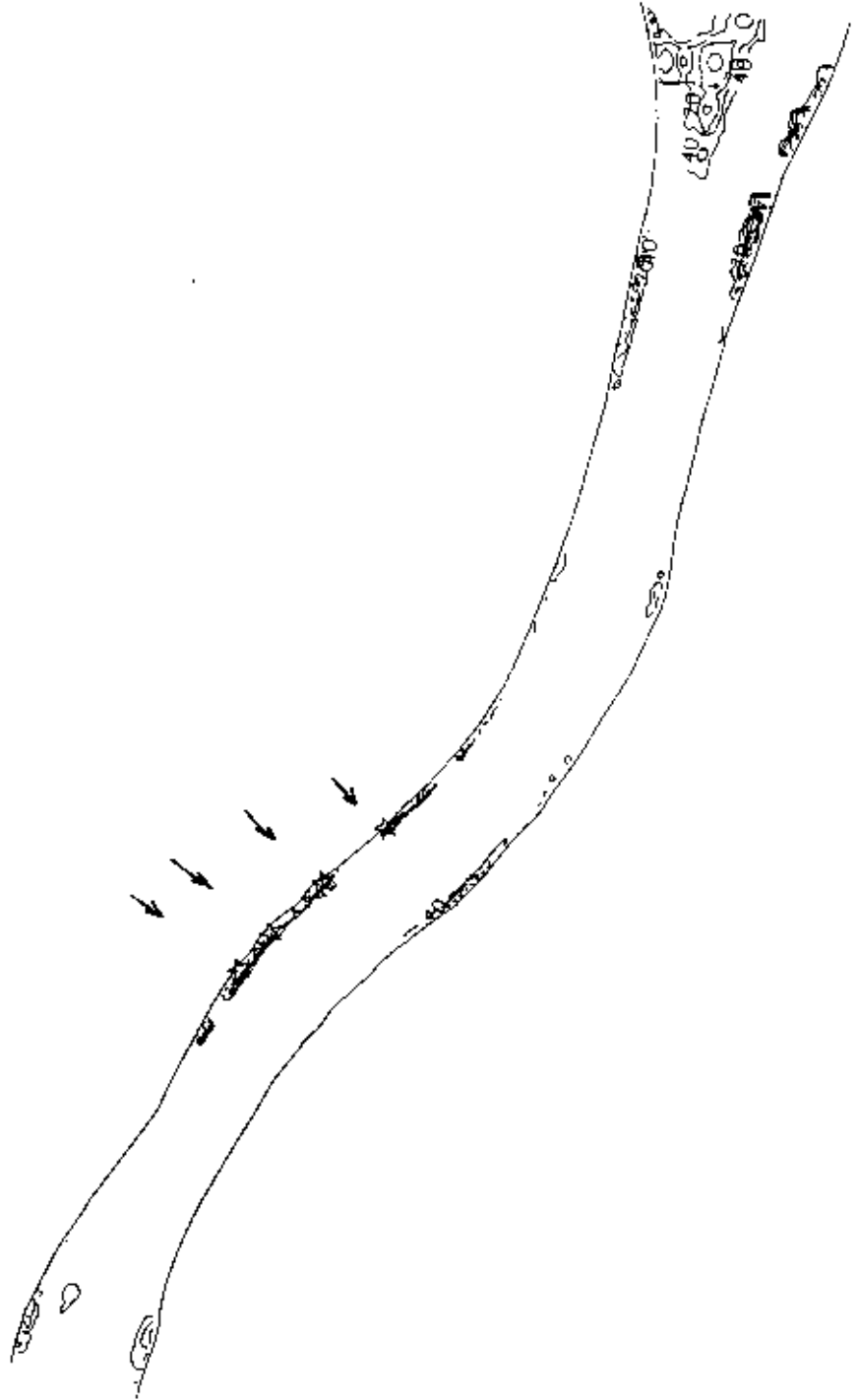


Figure 18 Comparison of simulation and data in sediment trap on 95/07/25

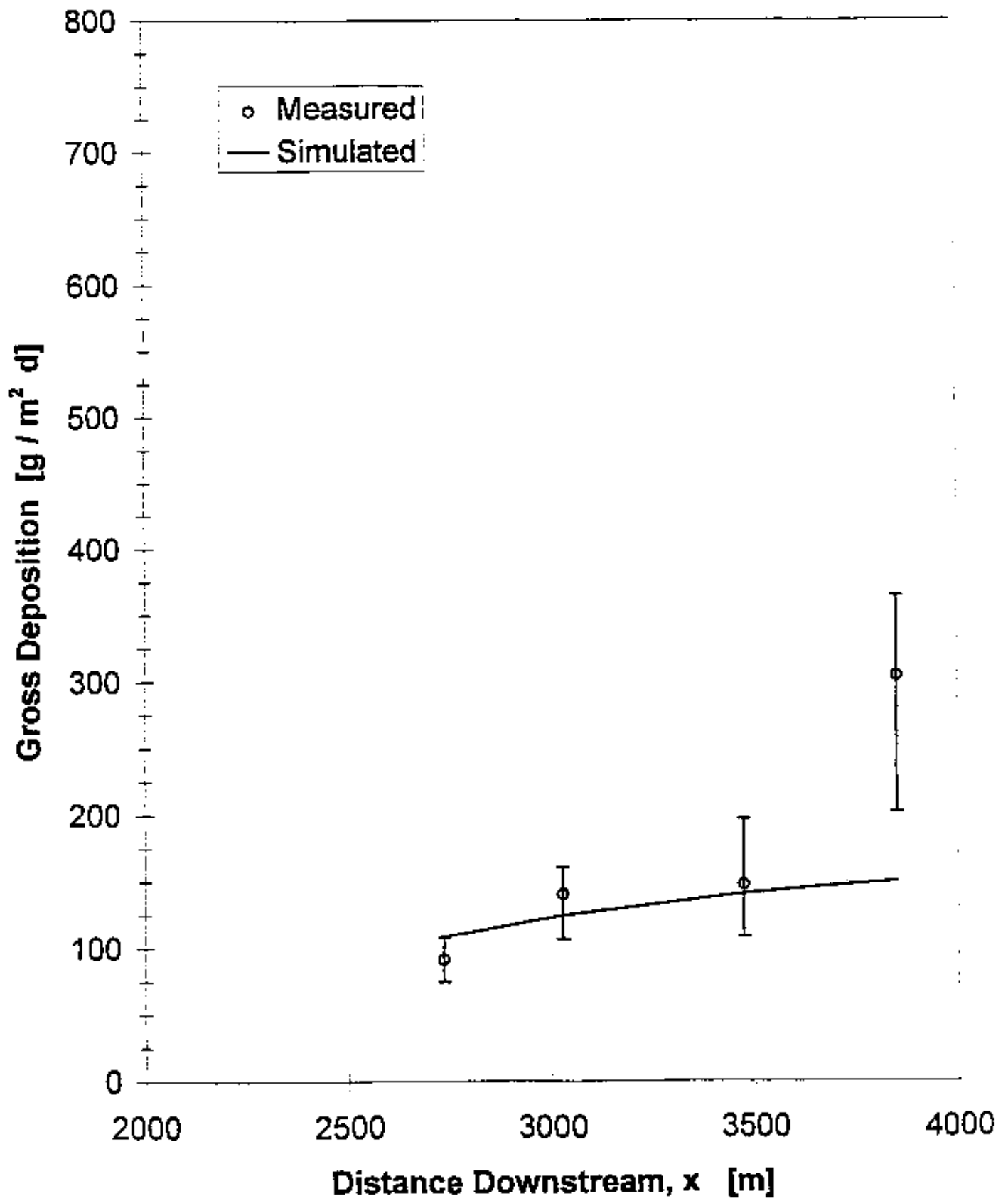


Figure 19 Net erosion area after 26 days, measured on 94/07/19 Max = 1.5 cm

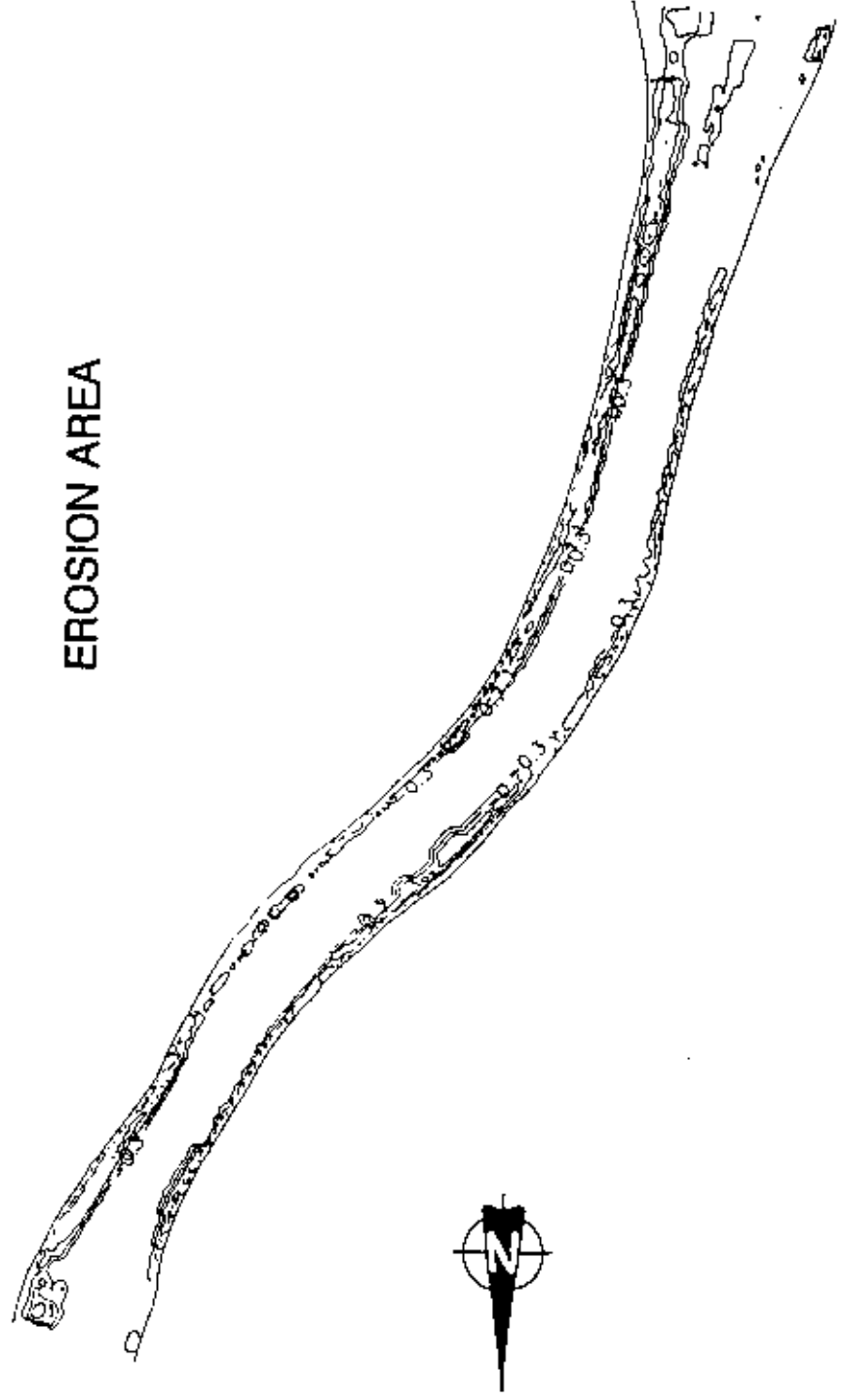
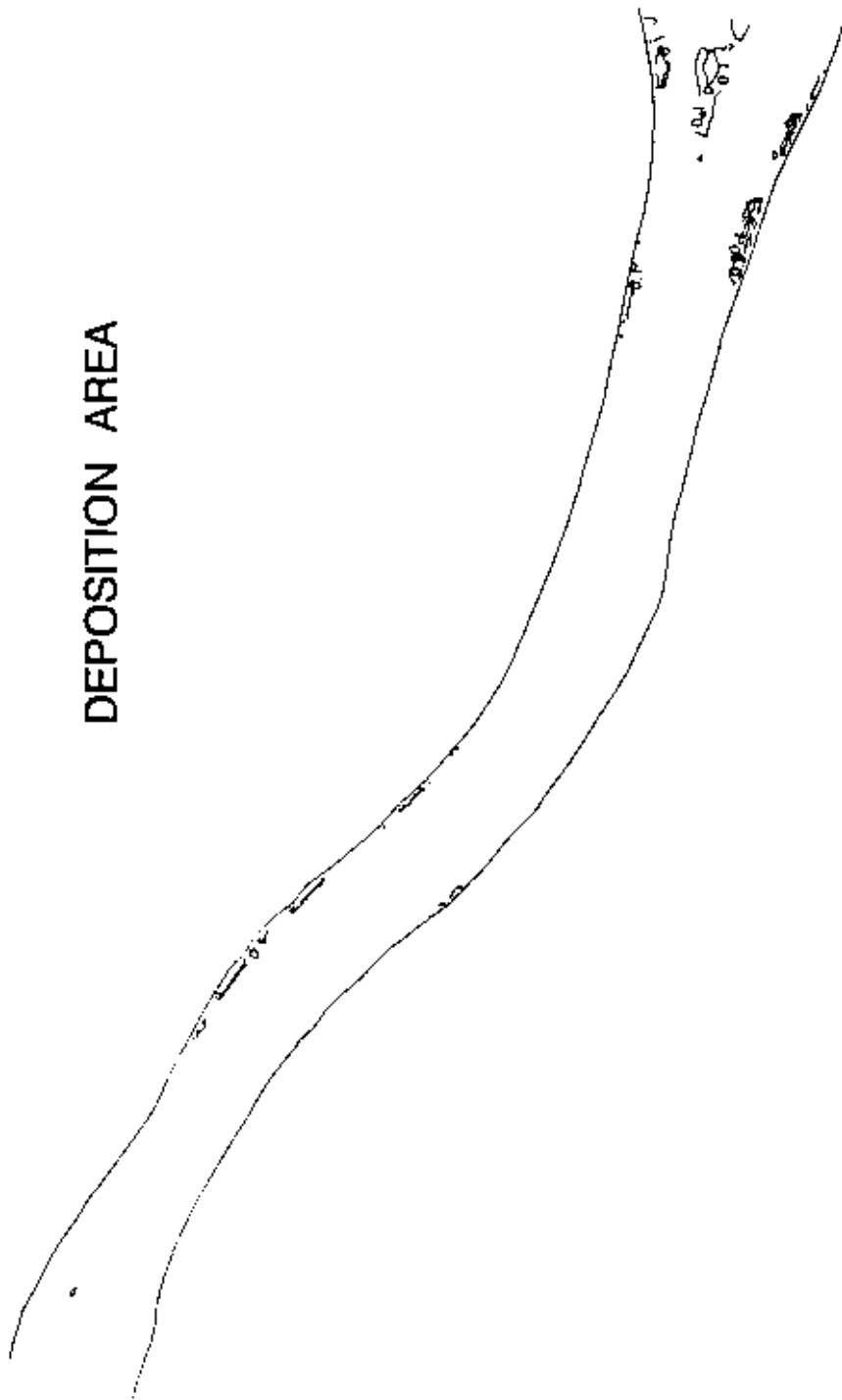
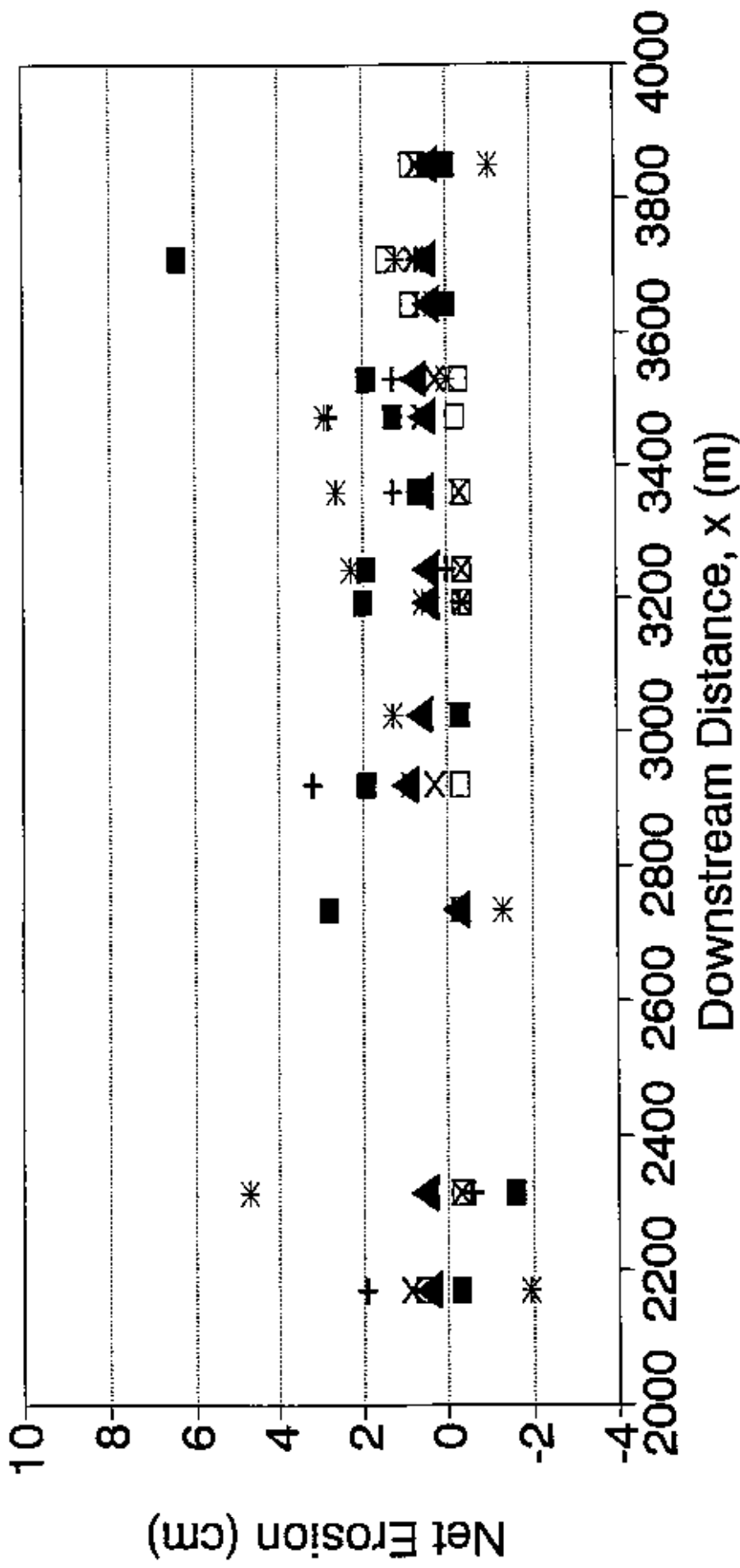


Figure 20 Net deposition area after 26 days, measured on 94/07/19 Max=0.8 cm



Model Output vs Measured Data

Figure 21 Comparison of simulation and measurement of rod data



- Meas'd - Nearsh + Meas'd - Mid. * Meas'd - Far
- Sim'd - Nearsh × Sim'd - Mid. ▲ Sim'd - Far

Figure 22 Increase in shear stress (N/m^2) due to wind (north 32 km/h)
(0.0 to 0.048 N/m^2)

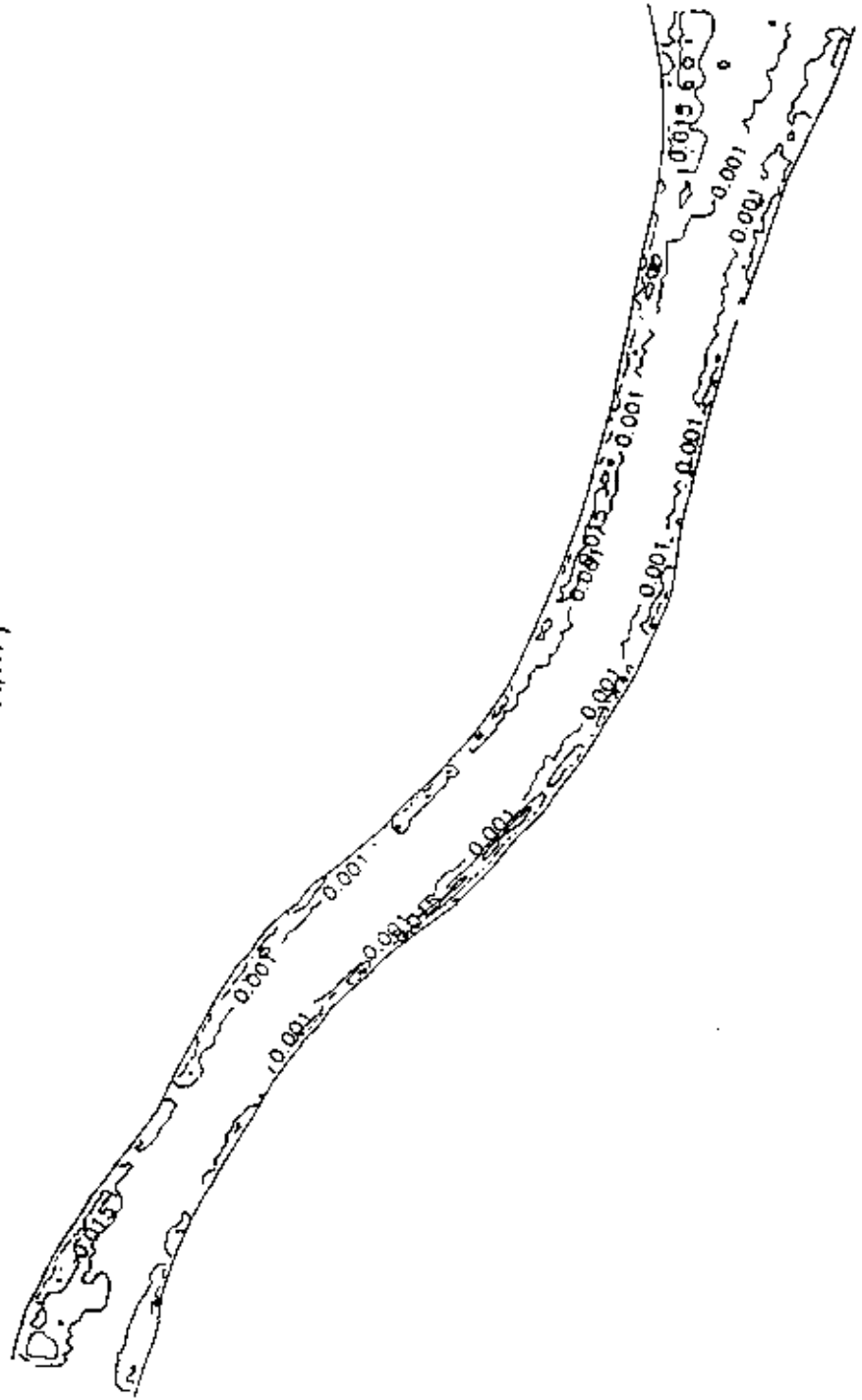


Figure 23 Shear stress (N/m^2) distribution for Q10 with average wind speed of 32 km/h (north)

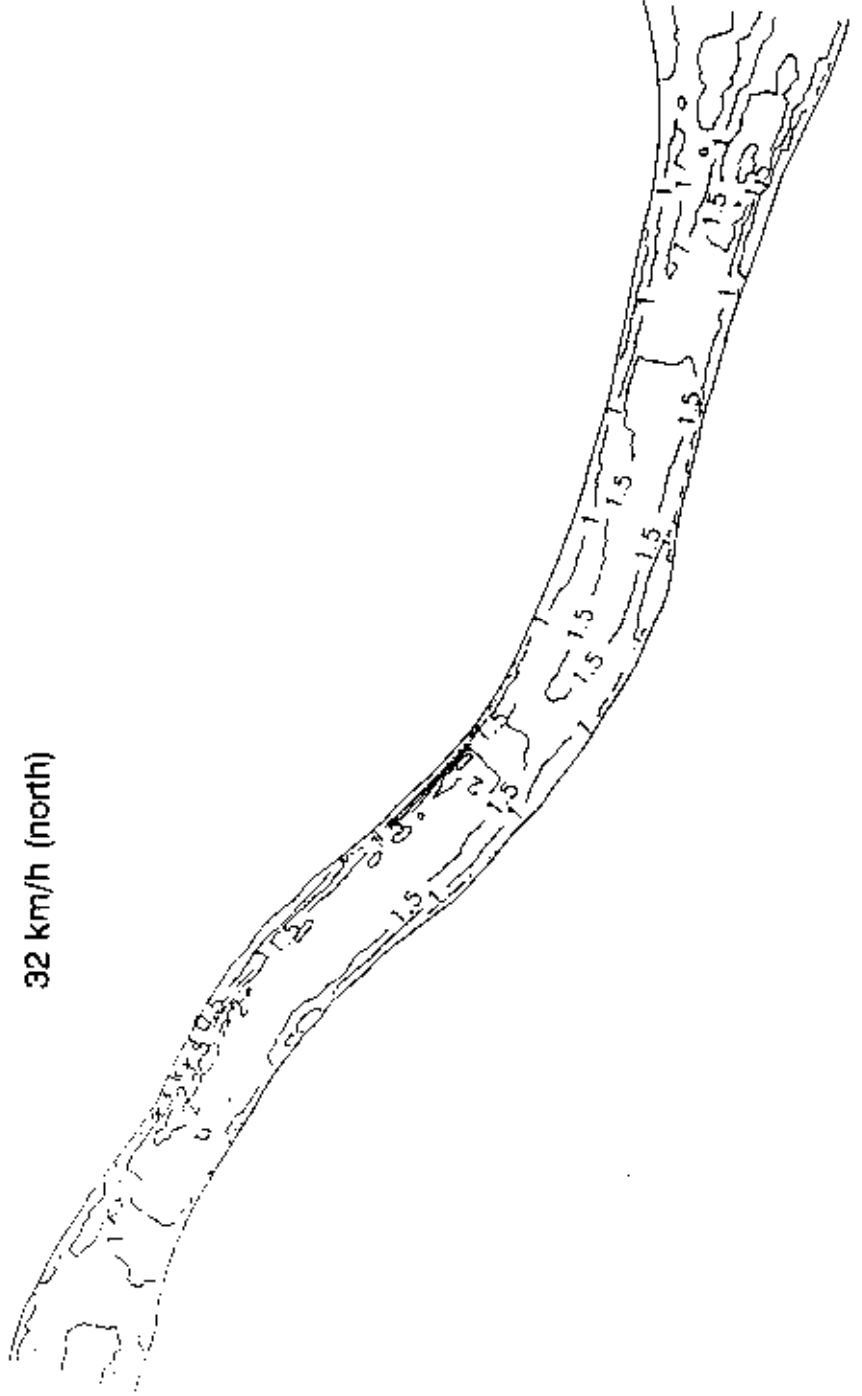


Figure 24 Shear stress(N/m^2) distribution for Q50 with average wind speed of 32 km/h (north)

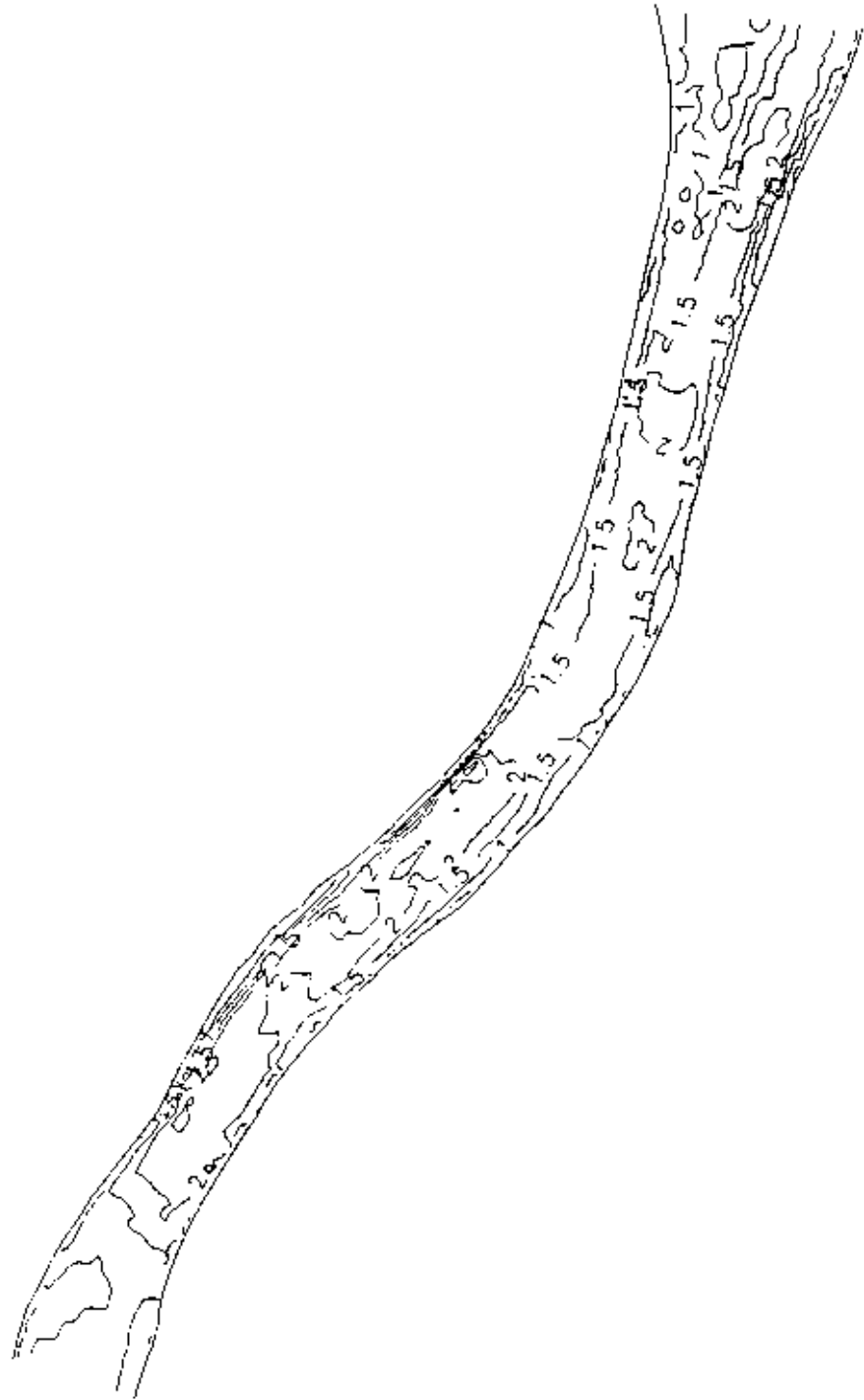


Figure 25 Shear stress(N/m^2) distribution for Q90 with average wind speed of 32 km/h (north)

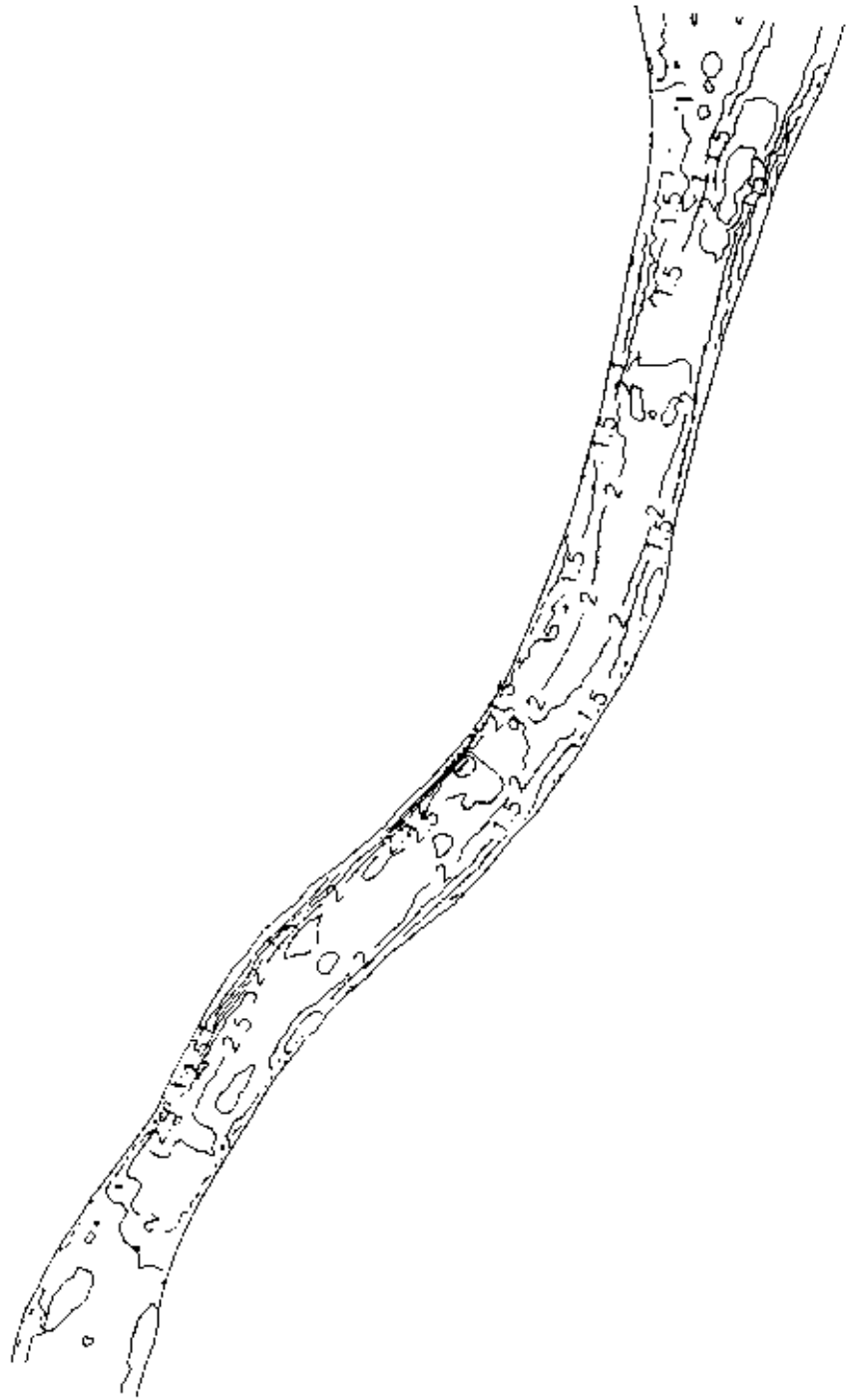


Figure 26 Maximum capacity of resuspension rate ($\text{g}/\text{m}^2/\text{s}$) for Q50

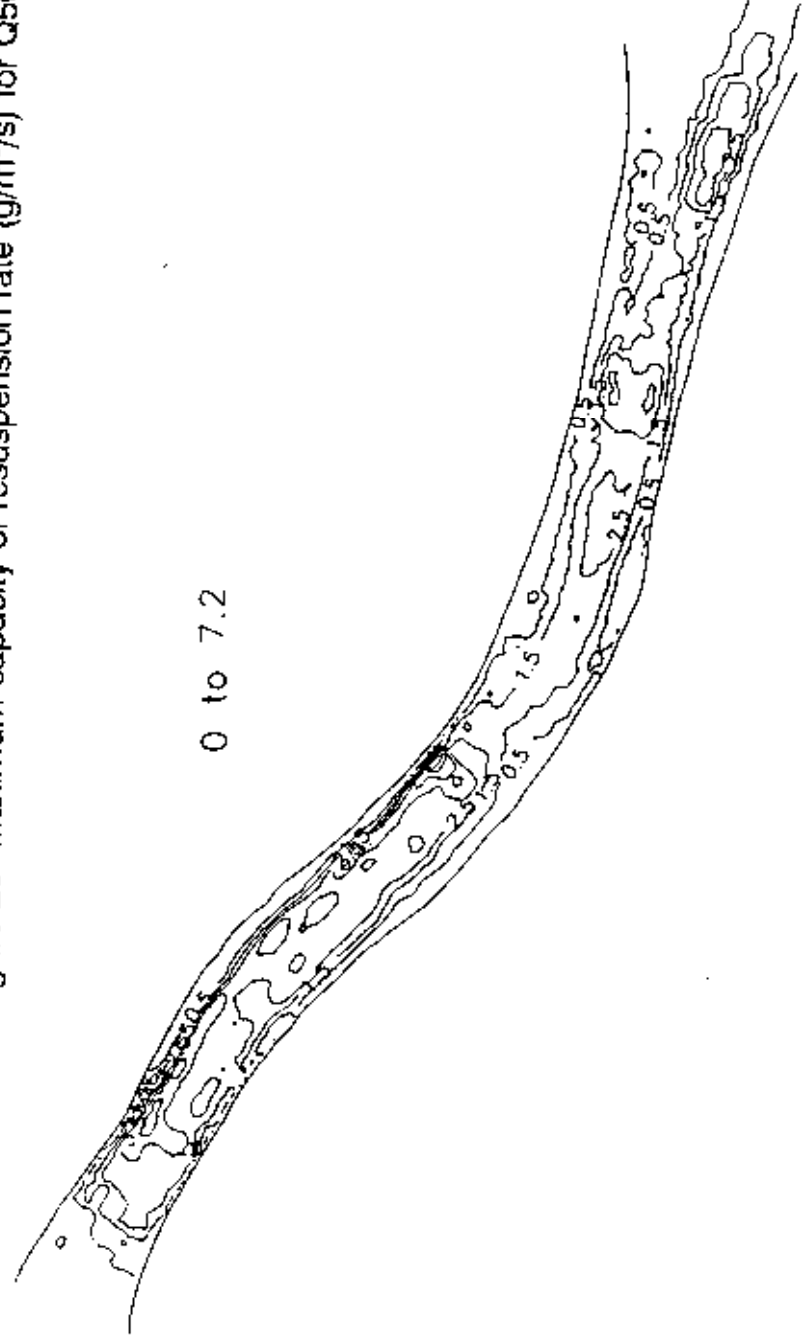


Figure 27 Minimum capacity of resuspension rate ($\text{g}/\text{m}^2/\text{s}$) for Q50

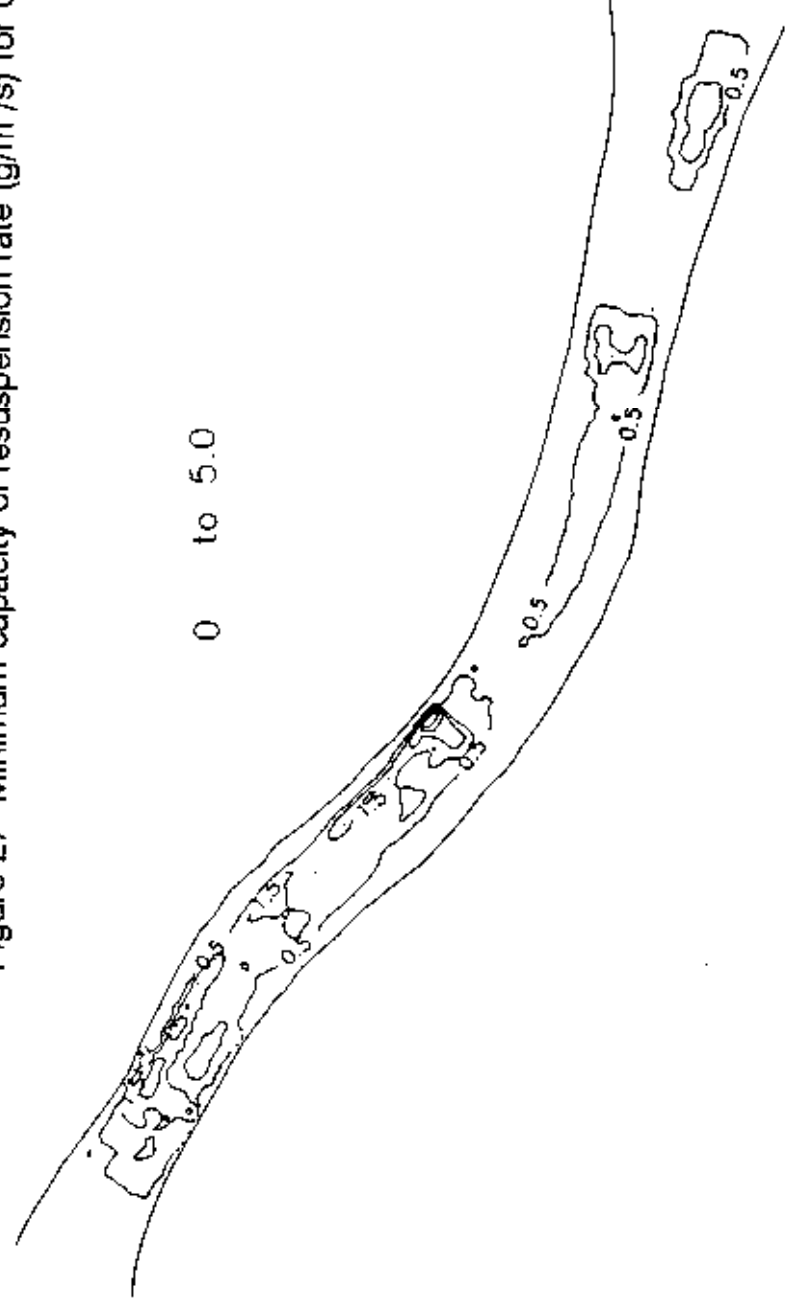


Figure 28 Surface velocity field for Q50

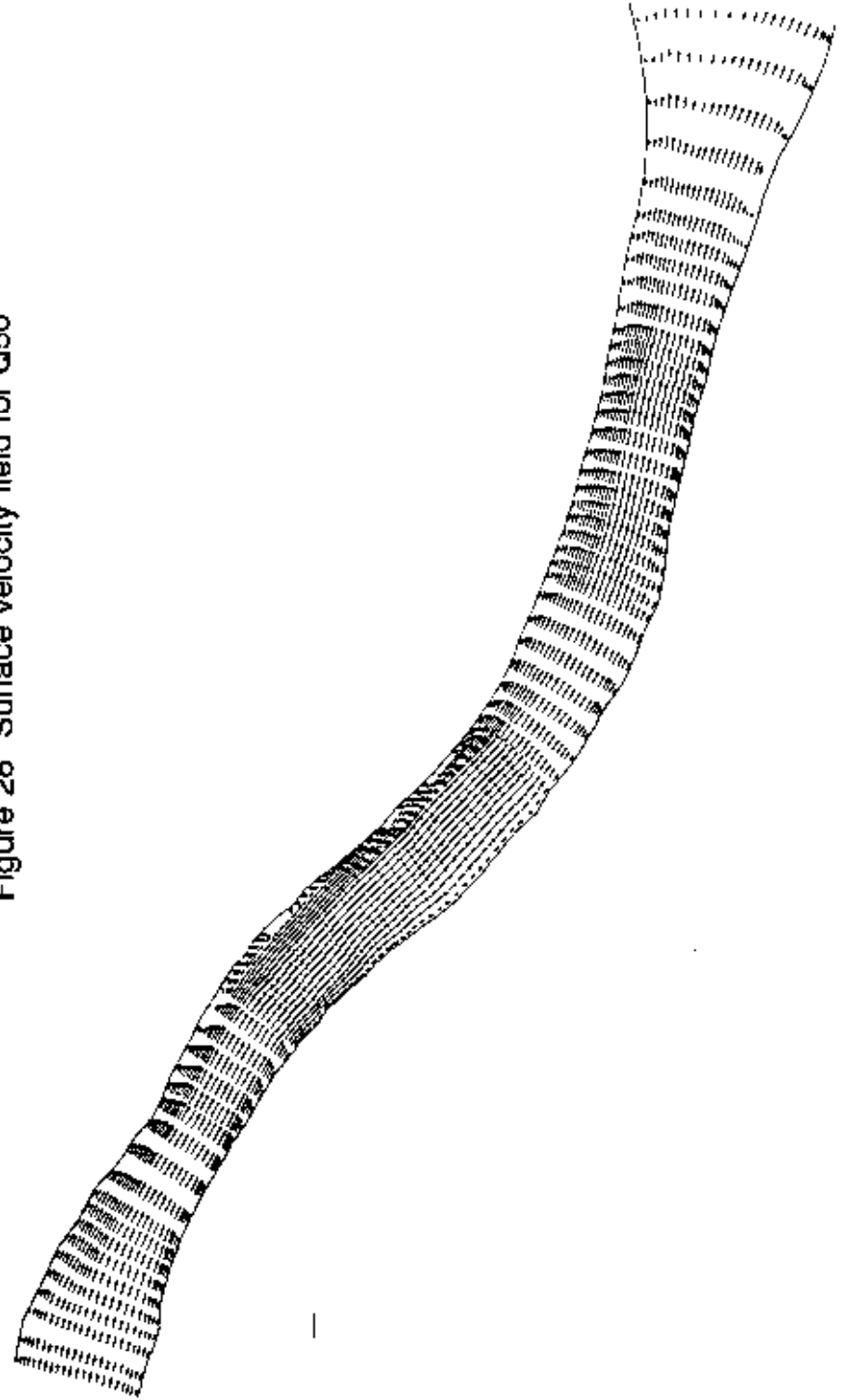


Figure 29 Near surface velocity field for Q50 under extreme wind condition

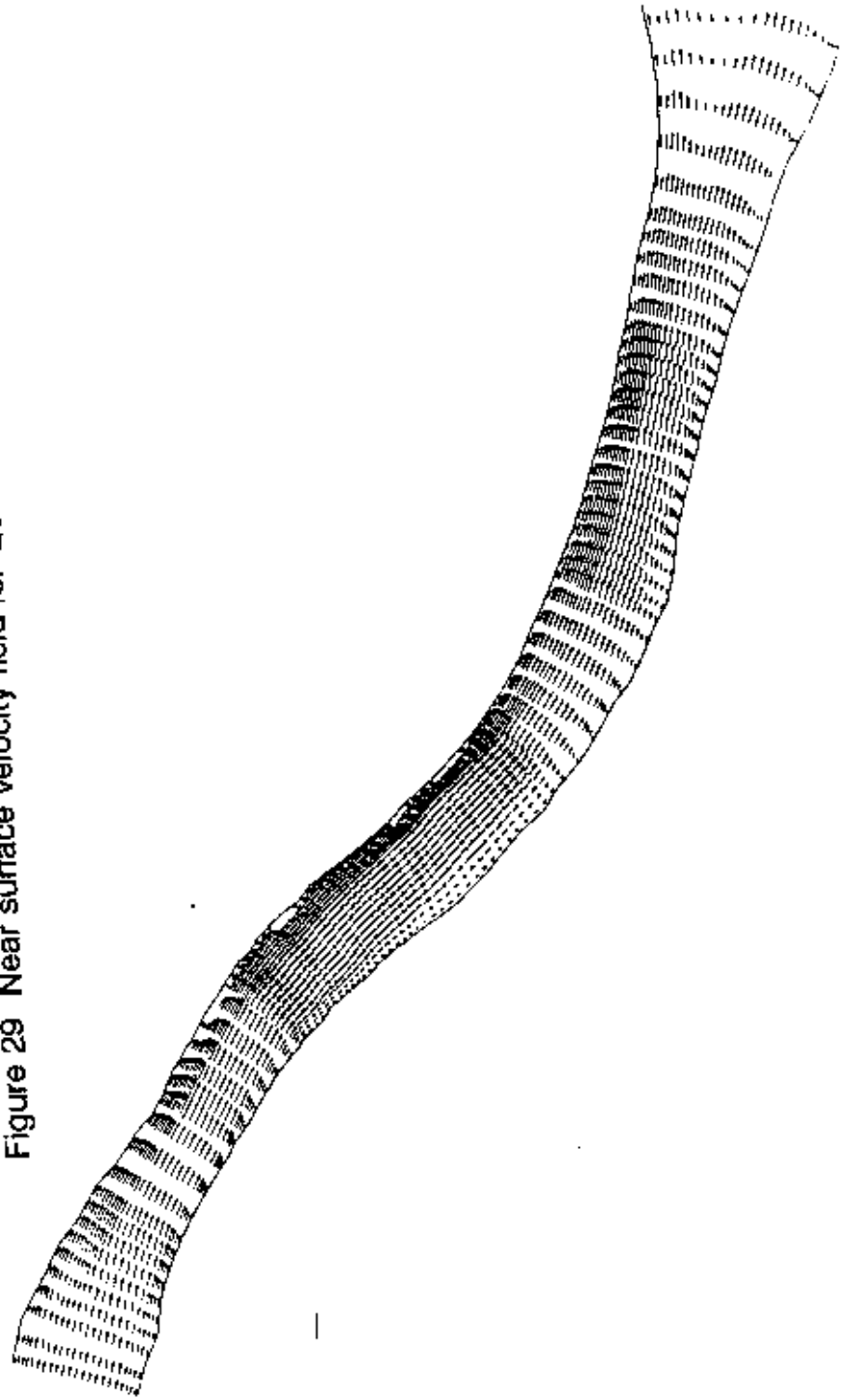


Figure 30 Increase in shear stress for Q50 due to extreme wind (0.0 to 2.1 N/m²)

